JᛔM PAPERS

Dependence of wake structure on pitching frequency behind a thin panel at $Re = 1000$

Arnab Kumar De[1] **and Sandip Sarkar**[2],†

[1]Department of Mechanical Engineering, Indian Institute of Technology Guwahati, Assam 781039, India

[2]Department of Mechanical Engineering, Jadavpur University, Kolkata 700032, India

We perform computations of wake transition behind a pitching panel using an immersed boundary-based method. At a Reynolds number $Re = 1000$, simulations are carried out over a wide range of pitching frequencies in the Strouhal number (St) range $0.2 \leqslant St \leqslant 2$, for two different aspect ratio panels, given by 0.54 and 2.38. Our results reveal appearances of a reverse von Kármán vortex street at a moderate pitching frequency, which bifurcates into two distinct branches connected by strands at higher Strouhal number. In addition, the larger-aspect-ratio panel exhibits an avalanche of large, tangled three-dimensional vortex structures for $St \geqslant 1.5$. We observe strong spanwise wake compression, for the larger-aspect-ratio panel, greatly influencing the secondary instabilities at increased pitching frequency. However, no direct relationship between the growth of secondary instabilities and the spanwise pressure gradient can be established. We show that an increase in St leads to a stable central region and renders a larger concentration of small-scale structures at the jet plane. The continuous wavelet transform shows complete synchronisation of the shed structure with the pitching Strouhal number of the low-aspect-ratio panel. The spectral characteristic for the high-aspect-ratio panel at $St = 1$ is found to be dominated by a narrow band of low-frequency cells. We observed the period-doubling phenomena in the spanwise cells during space–time reconstruction of the velocity signals. For the present ranges of St, both thrust and lift signals reveal a constant amplitude oscillation, the latter being double, in magnitude, the former. Both root-mean-squared thrust and lift coefficients grow with St and aspect ratio.

Key words: flow-structure interactions, vortex dynamics, vortex shedding

1. Introduction

The evolution of a vortex street during a fluid–structure interaction of a low-aspect-ratio pitching panel is of great importance owing to its variety of applications ranging from

biological to micro-air-vehicle locomotion and thermal management of electronic devices using piezoelectric fans (Buchholz & Smits 2006; Dong *et al.* 2010; Dewey, Carriou & Smits 2012; Agarwal *et al.* 2017; Bose & Sarkar 2018; Ebrahimi, Eldredge & Ju 2020). In these applications, the underlying propulsion mechanisms are primarily governed by low-aspect-ratio pitching motions, where the range of Reynolds number (*Re*) is 10^2–10^5 (Taira & Colonius 2009; Prince *et al.* 2010; Jafari *et al.* 2018; Nazari *et al.* 2018). A reverse von Kármán vortex street, characterising propulsive wakes, appears with an increase in the Strouhal number (*St*) (Oshima & Oshima 1980; Oshima & Natsume 1980; Freymuth 1988; Anderson *et al.* 1998). Four vortices are generated at each oscillation cycle if the vortices generated at the leading- and trailing-edge fall short of the optimal coalescence period. Koochesfahani (1989) reported this vortex shedding pattern under drag conditions, which is analogous to the one found past a freely vibrating circular cylinder (Williamson & Roshko 1988). The form of such vortices can be characterised as follows: single 'S', two single pair '2S', pair 'P', two pairs '2P', or a combination 'S + P', with flow remaining in a plane.

Experimental and computational studies past three-dimensional (3-D) flapping and pitching geometries reveals that the evolution of such a wake structure is highly dependent on the aspect ratio (*AR*) and *St* (Triantafyllou, Triantafyllou & Grosenbaugh 1993; von Ellenrieder, Parker & Soria 2003; Ghovardhan & Williamson 2005; Sarkar & Venkatraman 2006; Borazjani & Sotiropoulos 2008; Green & Smits 2008; Zhu & Shoele 2008). For *AR* = 0.27, experimental results on flexible panels resulted in approximately streamwise travelling waves which shed a vortex on the symmetry plane near the trailing edge at peak displacement (Buchholz *et al.* 2003). In the next half-cycle, a discrete vortex is formed by the rolling up the shear layers. This, along with the ensuing vortex, forms a counter-rotating vortex pair oriented transversely with the flow direction and results in a bifurcating wake (Buchholz *et al.* 2003). This wake event was later confirmed by the vortex structure of swimming *Anguilla rostrata* (American eels) at the bottom of a water channel (Tytell & Lauder 2004). Flow visualisation experiments on low-aspect-ratio propulsors revealed 2S- to a 2P-type wake transition in the case of reducing or enhancing the aspect ratio and *St*. A pair of countersigned vortices are found to shed at each pitching cycle, which later splits the wake by its transverse movement (Buchholz 2006). An undulatory swimmer's wake also showed transverse spreading and splitting into two pairs of vortices per pitching cycle (Hultmark, Leftwich & Smits 2007).

It has been shown that the most critical parameter in controlling the aerodynamic performance of low-aspect-ratio foils is the aspect ratio itself (Freymuth, Finaish & Bank 1987; Torres & Mueller 2004; Ringuette, Milano & Gharib 2007). Buchholz & Smits (2006) performed a series of flow visualisation experiments past a rigid pitching panel for *AR* = 0.54, *St* = 0.23 and *Re* = 640. They found that the wake is governed by the streamwise vortices produced from the edges of the plate consisting of the evolution of a 3-D von Kármán vortex street, which drives the wake along the centre of the plate in a manner similar to the axis-switching phenomena observed in non-axisymmetric jets (Dhanak & Bernardinis 1981). This spreading in the normal direction of the panel is coupled with a compression in the spanwise direction. The wake bifurcates with increasing *St* and generates a structure similar to those reported by Dong *et al.* (2010) and Guglielmini (2004). Later, Buchholz & Smits (2008) experimented with the effects of *Re*, aspect ratio and pitching amplitude on the vorticity dynamics and thrust performance for a low-aspect-ratio rigid pitching panel. At high $Re(10^4)$ and moderate aspect ratio and *St* they showed that the thrust coefficient increases with each of these parameters. In contrast,

the propulsive efficiency is sensitive to the aspect ratio, particularly for $AR < 0.83$. At higher St two oblique jets are observed, caused by bifurcation of the wake. These studies showed that wake bifurcation is not linked with a radical loss in the propulsion efficiency (Clark & Smits 2006).

Most of the previous research focused primarily on the experimental efforts of pitching and flapping foils. The corresponding 3-D numerical studies are limited; however, Blondeaux *et al.* (2005) carried out computations to investigate the wake characteristics past a flapping foil resembling fish-like locomotion. The numerical results of Dong, Mittal & Najjar (2006) for low-aspect-ratio ellipsoidal flapping foils revealed the convection of pair of interconnected vortex loops in the wake, which later evolved as twin oblique jets. Later, simulation results of Li & Lu (2012) for a 3-D flapping plate showed the dominance of flow structures near the plate on force and power generation. They also proposed a viscous vortex-ring model consistent with the kinetic energy evolution of a wake vortical structure. Liang & Dong (2015) performed proper orthogonal decomposition (POD) for low-Re flows over a low-aspect-ratio pitching-plunging 3-D plate. Their stability analysis results are classified into thrust- and lift-producing POD modes. The 3-D numerical analysis of Li & Dong (2016) for a low-aspect-ratio pitching-rolling plate showed the formation of alternating sign double-loop vortices at every half period of the motion. Subsequently, the direct numerical simulation results of Hemmati, Van Buren & Smits (2019) on the effect of trailing-edge shape for a small-aspect-ratio pitching panel showed strong 3-D effects for a concave trailing edge. Recently, Ebrahimi *et al.* (2020) reported a combined 3-D numerical and experimental investigation to examine the jet flows induced by a harmonically pitching plate in a quiescent fluid. There have also been a few promising 3-D numerical demonstrations comprising a highly deformable fish pectoral fin (Dong *et al.* 2010), a flexible low-aspect-ratio pitching plate (Dai *et al.* 2012), underwater flight of the manta (Fish *et al.* 2016), batoid fish-like locomotion (Thekkethil, Sharma & Agrawal 2020) and heaving motion (Visbal, Yilmaz & Rockwell 2013).

Table 1 lists relevant previous work on the rigid 3-D pitching of a rectangular panel with particular attention to the operating regime. Also, a few plunging, heaving and flexible cases are combined. It is apparent that most of these studies are primarily experimental, and that thus far numerical efforts have received relatively less attention. The pitching motions of 3-D rectangular foils reported in previous numerical simulations (Li & Lu 2012; Liang & Dong 2015) are restricted to $Re \leqslant 1000$, albeit with a fixed $St = 0.6$. In contrast, the current work is a new contribution and relevant study on unsteady bio-inspired propulsion, providing a much larger range of St ($0.2 \leqslant St \leqslant 2.0$) than prior simulations, at reasonably high Re. The detailed 3-D flow structures near the panel, and pressure data obtained from our computations, leverage the strengths of the simulations to produce results that may be more challenging for experiments. It is appropriate to mention that Cleaver, Wang & Gursul (2012) and Calderon *et al.* (2014) performed experiments on low-amplitude plunging NACA0012 aerofoil at high St, which resulted in wake flows very similar to those of pitching. They reported two lift-coefficient branches for high St at a condition where the angle of attack is less than or equal to the stall angle. The upper and lower branches correspond to the upward and downward deflected jets (Cleaver *et al.* 2012). They observed a long series of vortex loops generated from a long 'daisy chain' of interconnected trailing edge vortices (Calderon *et al.* 2014). The key research questions that have not been adequately addressed in the literature are as follows: (i) How does the enhancement in $St(> 1)$ change the different shedding regimes observed near the trailing edge of the pitching panel? (ii) What are the underlying mechanisms of the

Reference	Type	Motion	Re	St	AR	A/S	Mesh size ($N_x \times N_y \times N_z$)
Buchholz & Smits (2006)	Experimental	Pitching	640	0.23	0.54	0.31	—
Buchholz & Smits (2008)	Experimental	Pitching	640, $O(10^4)$	0.05–1.0	0.54, 0.83, 1.11, 2.38	0.070–0.63	—
Kim et al. (2017)	Experimental	Pitching, heaving	5×10^4	0.08–0.20	2.5, 3.5, 4.5	0.5–1.0	—
von Ellenrieder et al. (2003)	Experimental	Heaving, pitching	164	0.2–0.4	3	0.5	—
Panah, Akkala & Buchholz (2013)	Experimental	Plunging	10^4	0.2	1, 2, 4	0.3	—
Dai et al. (2012)	Numerical	Pitching, flexible	640	0.1–0.7	0.54	0.212	—
Visbal et al. (2013)	Experimental, numerical	Heaving	10^4, $10^3 - 2 \times 10^4$	$0.25/\pi$	2	0.25	$440 \times 469 \times 146$
Li & Lu (2012)	Numerical	Pitching	200, 500, 10^3	0.6	0.5–2.0	$\pi/6$	IB−LBM
Liang & Dong (2015)	Numerical	Pitching, plunging	200	0.6	0.64	0–0.577	$353 \times 258 \times 130$
Present	Numerical	Pitching	10^3	0.2–2.0	0.54, 2.38	0.07, 0.31	$400 \times 170 \times 170$

Table 1. List of previous studies for 3-D rigid pitching of rectangular panels. Here N_x, N_y, N_z are grids used in the numerical studies with lengths L_x, L_y, L_z. Note, few available 3-D numerical studies on pitching, heaving and plunging motions are mentioned together, whereas the present study primarily focused on the pitching motion only.

secondary instabilities associated with the wake compression? (iii) How does the pressure field behave near the trailing edge of the panel? (iv) What are the space–time behaviour and frequency events associated with the pitching motion at this St regime? (v) How do the force coefficients alter at these St ranges? In the present research, we have explored these questions using 3-D computations at $Re = 1000$ for $AR = 0.54$ and 2.38.

2. Physical system and numerical set-up

2.1. *Physical system*

The physical problem involves the pitching of a thin rectangular rigid panel about its leading edge, placed in a uniform left-to-right flow (U_∞), as shown schematically in figure 1. The coordinate system is so chosen that the x, y and z axes point in the streamwise, cross-stream and spanwise directions, respectively. The pitching motion about the z-axis is described by the angular displacement $\theta(t) = \theta_{max} \sin(2\pi f t)$ where f is the pitching frequency and the maximum angular displacement is given by $\theta_{max} = \tan^{-1}(A/2C)$ where A and C are the double amplitude and chord of the panel, respectively. The control parameters for the problem are the aspect ratio given by the span-to-chord ratio $AR = S/C$, Reynolds number based on chord $Re = U_\infty C/\nu$ and the imposed non-dimensional pitching frequency $St = fA/U_\infty$. We selected the panel geometry and computational domain to best reproduce conditions in the low-aspect-ratio pitching panel experiments by Buchholz & Smits (2006, 2008). Accordingly we limit $\theta_{max} = 5°$ and consider two aspect ratios $AR = 0.54$, 2.38 for a wide range of pitching frequencies $0.2 \leqslant St \leqslant 2$.

2.2. *Mathematical description*

The governing equations for the problem are the constant property, incompressible mass and momentum conservation laws. The thickness of the panel is taken as 3 % of the chord, which is placed in a domain that extends 15, 10 and 10C in the streamwise, cross-stream and spanwise directions, respectively. At the inlet, velocity is specified as $\boldsymbol{u} = (U_\infty, 0, 0)$ coupled with a zero pressure gradient $\partial p/\partial x = 0$. In order to keep the upstream feedback at a minimum level, a convective condition, given by $\partial(u, v, w)/\partial x = 0$ is prescribed at the exit plane with a gauge pressure $p = 0$. Boundary conditions at the shear-free vertical side boundaries read $\partial(u, v, p)/\partial z = 0, w = 0$, while the same marginally modifies to $\partial(u, w, p)/\partial y = 0, v = 0$ on the horizontal boundaries. Following the earlier pitching panel experiments (Buchholz & Smits 2008; Kim *et al.* 2017) and numerical studies (Liang & Dong 2015) together with the experimental measurements on biological locomotion (Taylor, Nudds & Thomas 2003), we fixed the Reynolds number at 1000. All the cases are started from a no-flow state and allowed to settle to a dynamic steady phase. Once attained, nearly thirty shedding cycles are used to compute the time-averaged field which is used for all the analysis shown in later sections including circulations, pressure gradient and force coefficients. The thrust, lift and spanwise force coefficients are defined as (Buchholz & Smits 2008), $C_{T,L,Z} = F_{T,L,Z}/(\frac{1}{2}\rho U_\infty^2 S C)$ where F_T, F_L and F_Z are, respectively, the thrust, lift and spanwise force components acting on the panel.

2.3. *Numerical set-up*

The conservation equations, mentioned in the previous section, are solved using a non-staggered finite-volume technique where special treatment is incorporated to
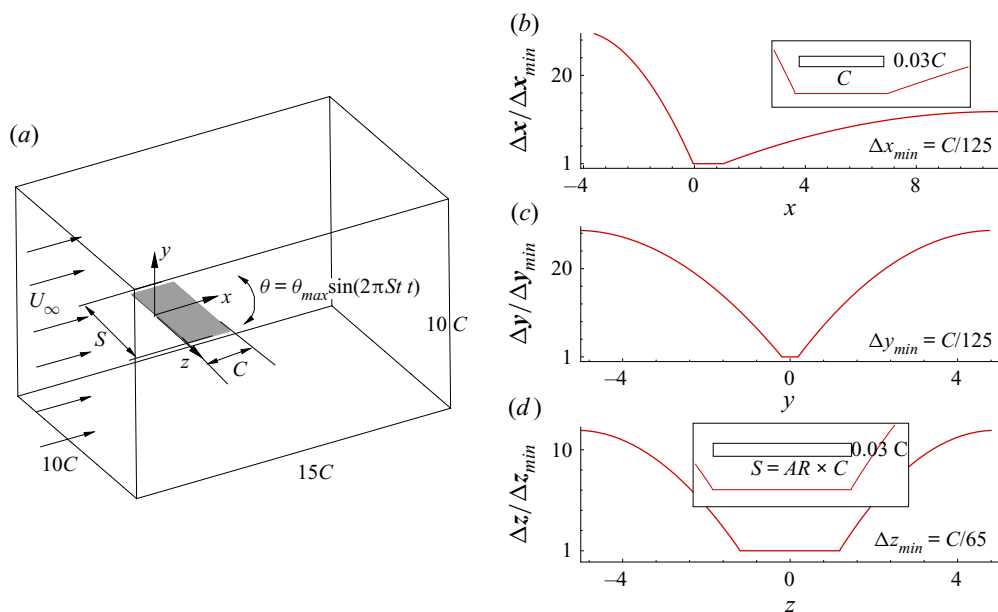
Figure 1. Schematic diagram showing a uniform flow past a rigid panel pitching about the leading edge with the extent of the domain. The variation of spatial grid resolution normalised by minimum mesh sizes $(\Delta x, \Delta y, \Delta z)_{min}$ along x, y and z directions are shown at the right-hand-side panel. In the inset, panel geometry is shown in all the three planes.

strengthen the velocity–pressure coupling. The second-order Adams–Bashforth scheme is used for the nonlinear convective terms, while the diffusive terms are handled implicitly using the Crank–Nicolson scheme in order infuse numerical stability into the overall time-integration strategy. All the spatial terms are approximated by second-order volume- or surface-integral approximations. The complex boundaries are resolved using the diffuse-interface immersed-boundary method (Pan & Shen 2009; De 2016, 2018) where a volume-averaged unified discrete equation is solved everywhere in the domain, relaxing the conventional variable reconstruction near non-conformal boundaries for sharp-interface immersed-boundary techniques. The panel, surface triangulated with approximately 32 000 and 78 000 triangular elements for $AR = 0.54$, 2.38, respectively, were found to predict the panel volume to nearly 1 % accuracy. A non-uniform Cartesian mesh with uniform grids in a volume that envelops the panel at all times was used for all the computations. The distribution of the grid spacing in all three directions is shown in the right-hand column of figure 1. The resulting sparse linear systems are solved to machine accuracy (10^{-8}) using the BiCGSTAB method, preconditioned by a highly scalable diagonalised version of Stone's strongly implicit procedure (SIP). The aforementioned numerical development has been achieved through a series of high-resolution complex geometry (De & Sarkar 2020*a*,*b*; Kushwaha & De 2020) simulations. All cases are simulated using a time step of $\Delta t = 5 \times 10^{-4}$, resulting in a maximum Courant number $Cu_{max} = 0.15$ for $St = 2$, which is found as a better trade-off between the speed and stability of the time-marching procedure. Total computational time for all the runs was nearly 0.16 million core hours on a 250 Teraflop SMP cluster.

In order to evaluate the effect of mesh refinement, the case with $AR = 0.54$ and $St = 0.6$ was tested on four progressively refined meshes starting with $M_1 = 200 \times 85 \times 85$ and
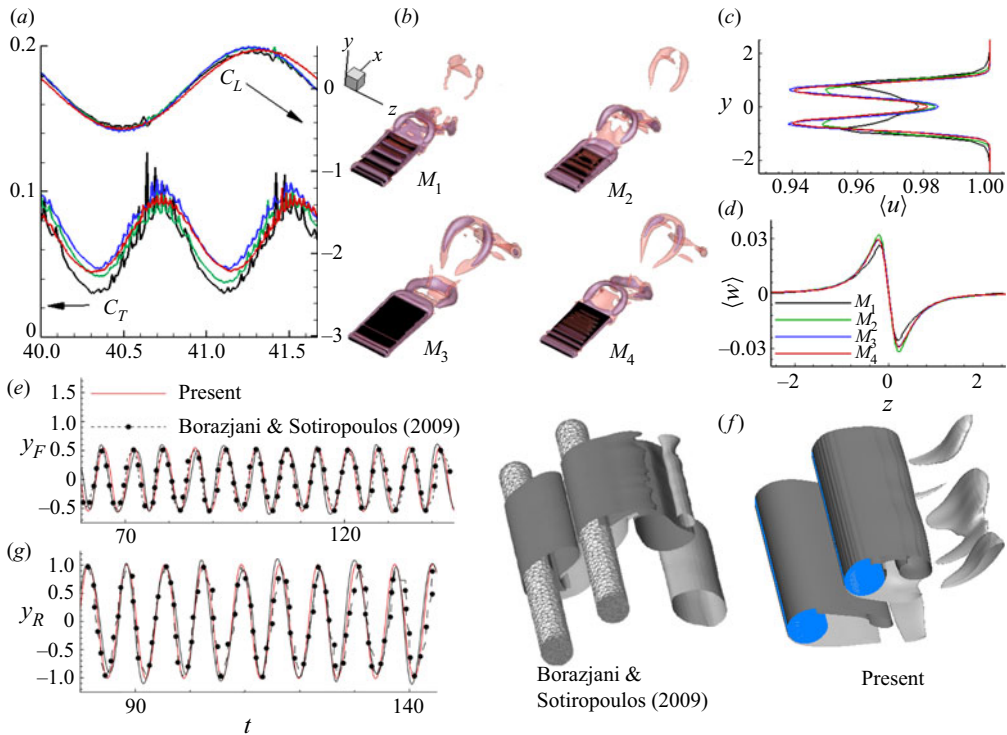
Figure 2. Mesh convergence test results for four successively refined mesh sizes M_1, M_2, M_3 and M_4 at $AR = 0.54$, $St = 0.6$. (*a*) Temporal evolution of the coefficients of lift C_L and drag C_D. (*b*) Perspective views of the 3-D instantaneous vortical structures visualised by the Q-criterion ($Q = 1$). (*c*) Variations of time-averaged streamwise velocity $\langle u \rangle$ in the cross-stream (*y*) direction. (*d*) Variations of time-averaged spanwise velocity $\langle w \rangle$ in the spanwise (*z*) direction. Panels (*a*), (*c*) and (*d*) have the same legends. Comparison of the present numerical set-up with Borazjani & Sotiropoulos (2009) for vortex-induced vibrations of a pair of rigid cylinders with (*e*) time evolution of the centroids of the upstream (y_F) and downstream (y_R) cylinders and (*f*) instantaneous spanwise vorticity ($\omega_z = \pm 1$) iso-surfaces.

increased 25 % in each directions while keeping a small Δt ($= 10^{-4}$). The time evolution of the thrust and lift coefficients, instantaneous vortical structure and time-averaged streamwise and spanwise velocities are shown for all the meshes in figure 2(*a–d*). Notwithstanding that an increase in mesh size small scale oscillations appear in the thrust coefficient, both the time-averaged velocities and force coefficients exhibit mesh convergence at the upper limit of the chosen grids. The horseshoe vortical structure becomes increasingly clear with refinements in mesh, and at the upper limit they become nearly identical at M_3 and M_4. In view of better resolution of the wake, the finest mesh given by $400 \times 170 \times 170$ ($AR = 0.54$) and $400 \times 170 \times 230$ ($AR = 2.38$) was chosen for all subsequent calculations. In addition, to check the validity of the present numerical model, we solved a multi-object fluid-structure interaction (FSI) problem for a pair of identical 3-D vibrating circular cylinders, and compared results with the numerical results of Borazjani & Sotiropoulos (2009). We carried out 3-D computations for a reduced velocity $U^* = 4$, mass ratio $m^* = 2$, and $Re = 200$. The time evolution of the centroids of the upstream (y_F) and downstream (y_R) cylinders are compared in frame (*e*), while frame (*f*) shows the instantaneous spanwise vorticity ($\omega_z = \pm 1$) iso-surfaces.

Agreement is found to be in the range excellent to reasonable, given the complexity and difference in the solution technique of the reference.

3. Results and discussion

We performed numerical simulations at $Re = 1000$ to assess the implications of varying St on the 3-D flow features of flow past a rigid pitching panel. We show the results by considering two illustrative values of aspect ratio in order to probe into the practical relevance of experimental conditions (Buchholz & Smits 2006, 2008) and biological locomotion (Richard 1958; Ellington 1984; Taylor *et al.* 2003). First, we demonstrate the alternations in the wake–vortex development under the combined influences of St and aspect ratio. Subsequently, we analysed the resulting circulation, secondary instability and discussed various other transition mechanisms.

3.1. *Overview of wake vortex topology*

In figure 3, we plot the instantaneous vortical structures with St for $AR = 0.54$ and 2.38. We visualised the wake vortices using iso-surfaces of $Q(=1)$ (Jeong & Hussain 1995). The vortex core region, which is depicted in red, has a smaller Q, which envelops the former. At $St = 0.2$, we observe a stable attached flow situation. A flat shear layer extends from the trailing-edge corners owing to its low-speed motion and is subjected to pure diffusion-dominated growth. However, at $AR = 2.38$, the streamwise length of the shear layers are found to be less than for $AR = 0.54$. With increasing St, we observe a wake transition. The wake patterns at $St = 0.4$ shows a slit-horseshoe vortex at $AR = 0.54$, and a bow-shaped structure at $AR = 2.38$. The vortex street remains attached to the panel owing to the induced velocity descending from the tip vortices at the trailing edge corners. At $St = 0.6$, the wake topologies for $AR = 0.54$ and 2.38 yield the formations of horseshoe and isolated bow-shaped vortices. Interestingly, at $St = 1$, the wake carries conformity with a reverse von Kármán vortex street for both aspect-ratio panels. The formation of an interlocked chain of horseshoe vortices is seen at $AR = 0.54$, whereas we find a bow-shaped vortex connected with secondary bridgelet-type structures (z-direction oriented structures that almost look like a corrugated surface on the panel) for $AR = 2.38$. Although such structures are drawn in a sketch in Buchholz & Smits (2006, 2008), experiments typically cannot resolve these near a body.

At $St = 1.25$, the streamwise vortex from the trailing edge for $AR = 0.54$ collapses within a shorter distance and splits, forming a bifurcating wake resembling a twin jet-type oblique flow pattern in the transverse direction. The horseshoe vortex shed from the trailing edge develops a perturbation before being bifurcated into a pair of jets. That, in turn, evolves to form a localised hairpin-like vortex signature, where the tip of the vortices is strong enough to keep the leading-edge vortex connected. In the spanwise direction, hairpins are convected in the transverse direction owing to self-induction. In contrast, at $AR = 2.38$, we observe an increased strength of the bridgelets forming more dipoles than at $St = 1$. The vortex filaments start interacting with each other via the thread-like connecting structures that connect two vortex filaments by wrapping around them. These structures eventually split farther downstream owing to spanwise instabilities (Visbal 2009) to form isolated pockets of vortex rings that rejoin with the small-scale bridgelets. We observe an analogous resemblance of wake structures between $St = 1.5$ and 1.25 at $AR = 0.54$. Higher stretching of the hairpin-vortex trains in the transverse direction is seen at $St = 1.5$. The heads of the hairpin vortices are loosely connected
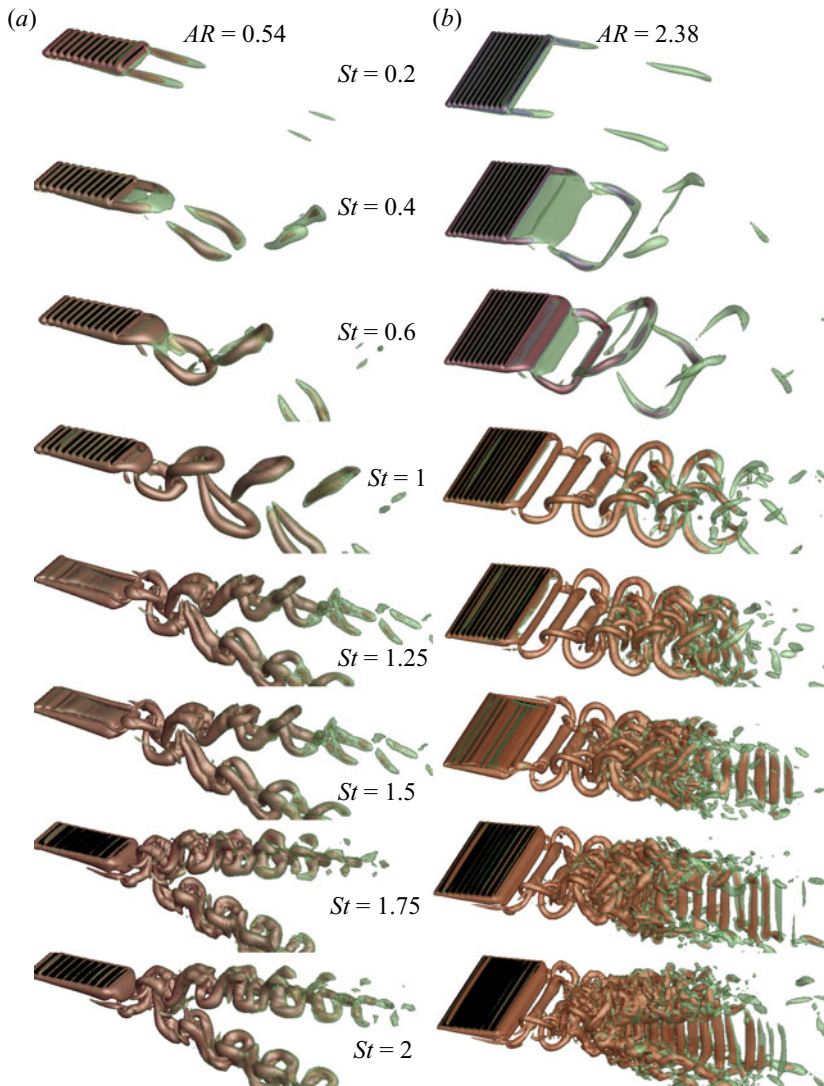
Figure 3. Influence of St on the wake vortex topology past a rigid pitching panel for $AR = 0.54$ and $AR = 2.38$. All 3-D perspective views of the vortical structures are visualised by plotting Q-criterion with $Q = 1$. Note, all the instantaneous Q-criterion structures are shown at the same dimensionless instant.

with the already shed preceding hairpin tails. The wake structure at $AR = 2.38$ exhibits rapid interactions of the threads, causing the bridgelets to grow into asymmetric vortex loops. The bridgelets undergo reconnection and, owing to self-induced motion, advect downstream. In this process, the regions of larger $|\boldsymbol{\omega}|$ in the primary vortex filament undergo rapid rotation and bring about a gross twisting of the vortex lines encompassing the bridgelets (Virk, Hussain & Kerr 1995). A further effect of strong spanwise instabilities split these bridgelets along with the primary vortex loops, ultimately culminating in the development of isolated packets of parallel strips advecting in the streamwise direction.

We observe that the overall vortex dynamics become even richer and more complex beyond $St > 1.5$. For $St = 1.75$, we see that the hairpin vortices at $AR = 0.54$ transmute to ring-like vortex structures, yielding two distinct chains of alternating vortices each

engulfed by the next downstream of it (Dai *et al.* 2012; Li & Lu 2012). The vortex rings are oriented primarily in the streamwise direction and interlocked by hairpin-type vortex legs. As expected, the spanwise instabilities contribute to the initial circular core of the rings and deform into braid-like structures. A further increase in *St* causes the rotation of the vortex rings, which are inclined in the transverse direction at $St = 2$. The rings travel downstream under self-induction, which again deform and recede via spanwise instability-driven cross-diffusion. For $AR = 2.38$, the bridgelets undergo successive reconnection and stretching with the primary shed vortices triggered by the strong spanwise instability at $St = 1.75$. These reconnections encourage the evolution of swirling rings of vortices and then again deform into complex structures, cause the generation of smaller vortex filaments, and thereby promote the wake into an avalanche of 3-D vortex structures. Interestingly, $St = 2$ yields a much complicated wake topology, showing a transverse asymmetrically bifurcated wake rolling over the parallel strips. The isolated arrays of parallel strips are now produced at a much earlier stage and are broadly dominated by the remaining vortex filaments that survived during the wake cloud formation. Irrespective of aspect ratio, the streamwise spacing of the vortex structures is reduced with increasing *St* (Dai *et al.* 2012; Li & Lu 2012).

In figures 4 and 5 we describe periodic evolution of the vortex street based on the *Q*-criterion for $St = 0.6, 1$, at $AR = 0.54$ and 2.38, respectively. In a complete pitching cycle, the temporal evolution of vortices corresponding to the instances $(a–f)$ are indicated in the insets on θ, C_T and C_L time series. At $St = 0.6$, the pitching cycle starts with formations of the horseshoe ($AR = 0.54$) and bow-shaped ($AR = 2.38$) vortices without connecting their tips by peeling off the spanwise shear layers accumulating at the trailing edge. The tip of the vortices at this lower *St* lack strength and, as a result, the mutual induction process responsible for linking the tips deteriorates. It may be pointed out that the vortex connections visualised depend on the values of *Q* plotted for the iso-surfaces. A smaller *Q* value would probably show increased connections (in agreement with the point that they are weaker here). During the upward stroke ($\theta \rightarrow \theta_{max}$), the shear layers accumulate to form a convex shape and cause an extension of the panel surface farther into the wake, allowing an auxiliary growth of the vortices before detachment. The instant the vortex strand grows into its developed stage, the strand connecting the boundary layer with the local vorticity extreme experiences a strong strain rate dominated constriction mechanism. In effect, the strand commences a detachment process from its source near to $\theta \approx \theta_{max}$. This is followed by pinching off a coherent horseshoe (or bow-shaped at $AR = 2.38$) vortex in the upward direction of the panel owing to upward-induced velocity near to $\theta \approx \theta_c$, which gradually moves in the streamwise direction with the downstream advection of the flow. It is worth mentioning that the area over which this constriction process occurs is governed by the positive strain-rate parameter $\gamma > 0$ where $\gamma \approx \text{tr}(D^2)$ and the rate-of-strain tensor $D = (\nabla \boldsymbol{u} + (\nabla \boldsymbol{u})^{\text{T}})/2$ (Biswas & Sarkar 2009).

The vortex formation during the downward stroke ($\theta \rightarrow \theta_{min}$) follows an analogous route, except that the downstream induced velocity causes the shed vortical structure to roll towards the downward direction of the panel at approximately $\theta \approx \theta_f$. At $AR = 2.38$, the disconnected tip of the bow-shaped vortices start to interact with the legs of the already shed vortices post detachment. This interaction causes a gradual reduction of the downward velocity induced by the shed vortices thereby forming bridgelet-type structures at higher *St*, whereas at $AR = 0.54$, isolated horseshoe vortex structures become apparent. Note that we witness the formation of two vortices per pitching cycle for both *St* (Buchholz & Smits 2006, 2008). At $St = 1$, the pitching cycle results in the
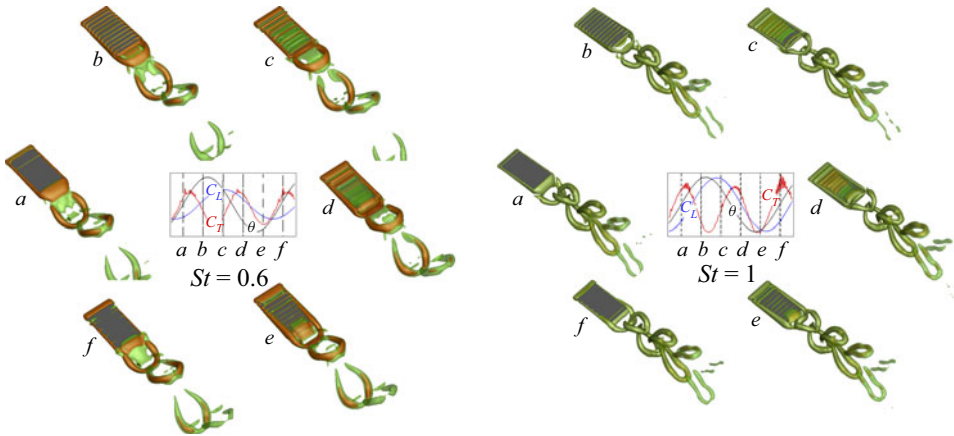
924 A33-10

Figure 4. Perspective views of the 3-D periodic vortex shedding cycle showing $Q = 1$ surfaces at $AR = 0.54$ for $St = 0.6$ and 1. The temporal evolution of vortices from the trailing edge of the panel is shown in the instances $(a–f)$ indicated on the time series of C_T, C_L and θ in the insets.
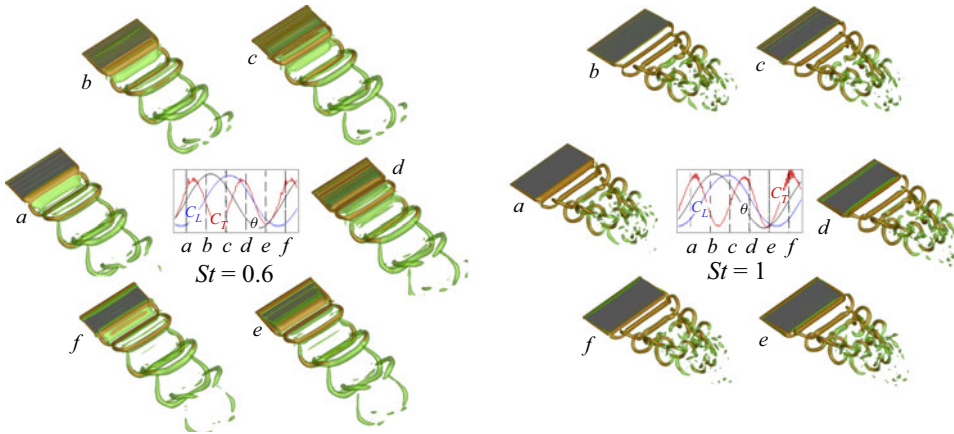

Figure 5. Perspective views of the 3-D periodic vortex shedding cycle with $Q = 1$ surfaces at $AR = 2.38$ for $St = 0.6$ and 1. In the insets, the temporal evolution of vortices from the trailing edge is shown in the instances $(a–f)$ indicated on the time series of C_T, C_L and θ.

formation of a chain of horseshoe and bow-shaped vortices interlocked together to emerge as a reverse von Kármán vortex street for $AR = 0.54$ and 2.38. The overall formation dynamics are analogous to the one at $AR = 0.54$, although the period is smaller in terms of the occurrence of wake vortex structures for $St = 1$. The bow-shaped structure shed outward from the trailing edge is connected with the hitherto shed vortices with secondary bridgelet-type structures. This occurs owing to the mutual induction of instantaneously generated threads, which advect faster than the primary vortex loops. As the vortices convect farther downstream, the bridgelets split owing to the development of the spanwise instabilities, and, in consequence, leave behind discrete packets of vortex contrails. Farther downstream the wake appears weaker and dissipated for $St = 1$. Nevertheless, the vortex configuration governs the extent of the wake coherence and is regulated by the shear layers released from the trailing edge. We also observe from the insets that regardless of aspect ratio and St, that θ_c, corresponding to the separation of the trailing-edge vortices

during upward stroke, is always nearer to the maximum lift ($\sim C_{L_{max}}$) and minimum thrust ($\sim C_{T_{min}}$) point. In contrast, we find an inverse relationship during the downward stroke of the pitching cycle.

3.2. *Circulation of the wake*

We calculated the dimensionless circulation along the spanwise $\Gamma_z = \int_{\Omega_z} (\nabla \times \boldsymbol{u}) \cdot \hat{n}_z \, d\Omega_z$ and streamwise $\Gamma_x = \int_{\Omega_x} (\nabla \times \boldsymbol{u}) \cdot \hat{n}_x \, d\Omega_x$, directions using the time-averaged velocity (see §2.2), where $\hat{n}_x$ and $\hat{n}_z$ denote unit normal vectors along x and z directions. We computed circulation values for the domain-independent regions $\Omega_x \equiv (y \times z) \equiv \{(0, 4) \times (0, 3.5)\}$ and $\Omega_z \equiv (x \times y) \equiv \{(1.1, 8) \times (0, 4)\}$. It should be noted that Γ_x and Γ_z only account for half the span and transverse plane (because the circulation over the entire span or plane would be zero).

In figure 6, we show the dependence of Γ_z and Γ_x on St for different aspect ratios. In general, the circulation strength increases with increasing St, and is a strong function of AR. We observe from figure 6(a) that at $St = 0.2$, Γ_z decreases monotonically from the centre of the panel to its local minimum nearer to the edge. After that, it increases progressively to zero at approximately $z \approx 0.6$, a region beyond the zone of influence of the shed vortices. For the negative directional growth in Γ_z, see figure 3, the attached shear layers formed at the trailing edge are seen to play their role. At $St = 0.2$, only a few circulation loops, distributing a larger spanwise area evolve at the trailing edge with a strong localised counter-clockwise rotation. This leads to an enhancement of the circulation strength and makes the region prone to negative growth. Beyond the minimum point, the overall circulation strength reduces owing to the reduction in spanwise diffusion of the shear layer. Therefore, the local circulation shows an asymptotic increase in the positive direction until a zero value is reached near the zone of influence. We observe that Γ_z curves essentially collapse across z for $St > 0.6$. At $St \geqslant 1$, the formation of multiple tangled vortices are more enhanced, and, through mutual inductions, eventually results in a reduction in circulation strength.

In contrast to $AR = 0.54$, we observe an entirely different trend of Γ_z at $AR = 2.38$. Figure 6(b) shows that the characteristic behaviour of Γ_z for $St = 0.2, 0.4$ is negative at $AR = 2.38$ and does not change with the aspect ratio. The value of Γ_z is nearly flat and only shows higher values (negative direction) closer to the edge of the panel. At $St > 0.6$, near the central region of the panel, Γ_z exhibits positive maxima, but shows negative minima for $AR = 0.54$. In addition, the spanwise variations in Γ_z at $AR = 0.54$ become increasingly higher, although, at $AR = 2.38$, it drops along z. Hence, the character of the wake for these aspect ratios is different from that expected from the measured circulation. Interestingly, the boundary point of the wake zone of influence ($\Gamma_z = 0$) moves towards the central region of the panel with increasing St, indicating that wake compression is prevalent owing to the competitive effects between aspect ratio and St. Accordingly, we observe a much smaller zone of influence at $AR = 2.38$ than $AR = 0.54$ for larger St. For $St > 0.6$, an increased secondary instability causes fluid particles at the edge to break up and approach the central wake region. This triggers a wake compression by increasing the spanwise movement of the flow at higher St. The flow attempts to compress and converge towards the central region, and a negative pressure region along the wake width develops. As a result, the intensity of w, which is responsible for wake compression, increases, thereby causing the wake activity to be constrained within a narrow band in the spanwise direction.
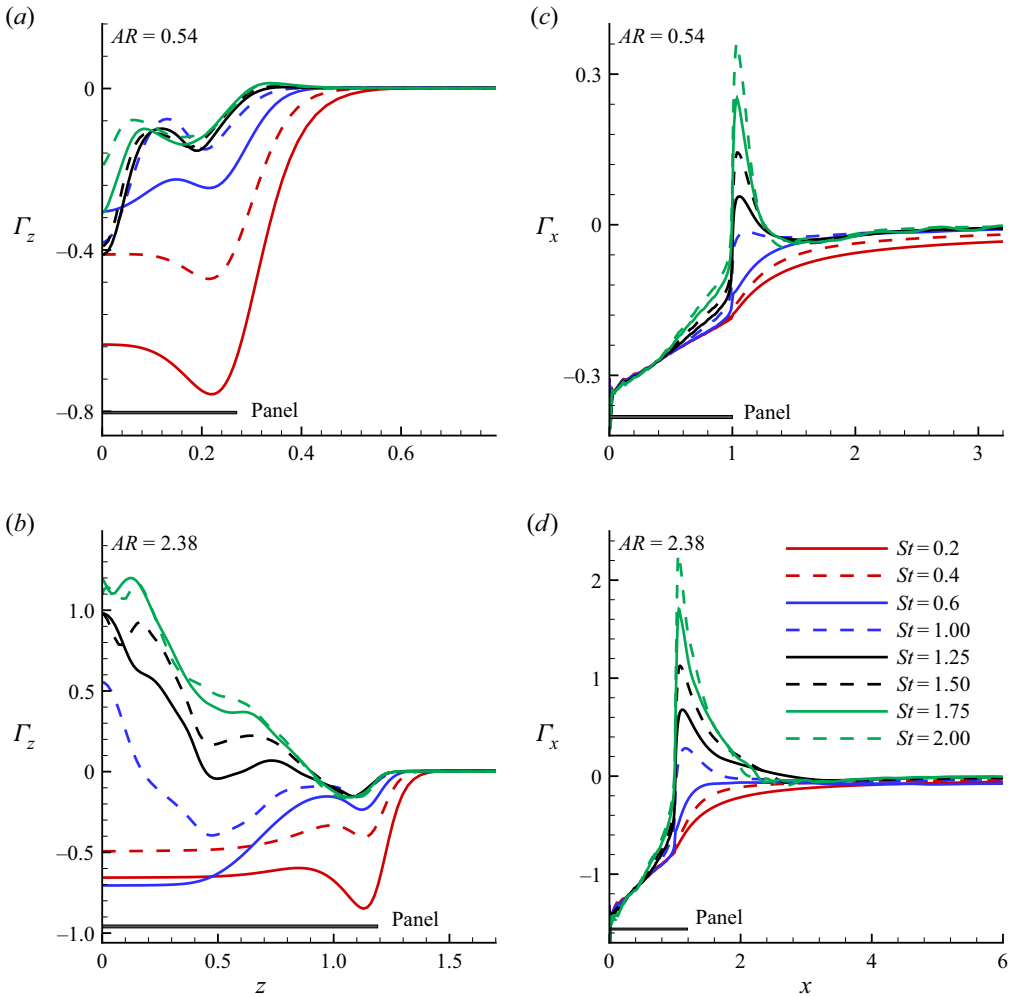
Figure 6. Dimensionless wake circulation along the spanwise (Γ_z) and streamwise (Γ_x) directions for various *St*. Results are shown at aspect ratios of (*a*,*c*) 0.54 and (*b*,*d*) 2.38, respectively. The proportionate panel dimensions corroborating each aspect ratio are also indicated.

The wake tends to form a concentrated core region constituting intense localised vorticity distribution. This may be conditional on large *St* situations where the vorticity has higher strength. In the compressed wake, the velocity at the central region is less than that of the side wake region. The side wake remains unperturbed, but the core region constituting the compressed wake moves very slowly. This results in less diffusion of the compressed vortices, because for diffusion to occur vortices have to encounter a high-velocity region. Again, as the vortices are compressed, the chances of cancellation of positive and negative vortices becomes lower, yielding a fewer number of high-intensity circulation cells within a smaller area. Therefore, the core region possesses the maximum circulation magnitude, which is shown in figure 6(*b*).

We observe from figure 6(*c*,*d*) that Γ_x increases from the leading edge of the panel to its saturated value of $\Gamma_x = 0$ far downstream. The circulation curves for $0.2 \leqslant St \leqslant 0.6$ exhibit smooth variations, whereas, for $St > 0.6$, we notice a discontinuity in the

$\Gamma_x - x$ distribution, which yields a sudden jump near the trailing edge. We see that the streamwise variation of Γ_x from the leading edge grows almost linearly without showing any discernible differences with changing St. This phenomenon is attributed to the development of a sheet-like unsteady shear layer at the hinged plane, shed from the leading edge, which is found to be St-invariant. Near the trailing edge, a bifurcation in the Γ_x distribution is attributable to higher values of angular velocity of the isolated vortex structures just after detachment. This eventually leads to an enhancement of linear velocities at higher St. The overall influence culminates in a discontinuity in the Γ_x profile. Beyond the region of discontinuity, the formation of small-scale vortex structures, of lower circulation strength, are the sole contributors of a progressive decay of Γ_x. As a result, there is a gradual reduction of Γ_x up until a threshold streamwise location is reached, beyond which Γ_x shows axial invariance. At this point further cascading of circulation loops, owing to secondary instabilities, nullify each other, which results in $\Gamma_x = 0$.

In figure 7(*a*) we show the dependence of Γ_z as a function of St at the central plane ($z = 0$) and edge ($z = S/2$) of the panel for $AR = 0.54$, 2.38. We found that an increase in St increases the circulation strength. Beyond $St > 0.6$, there is a wake compression with fewer heavily squeezed high-intensity circulation cells at the central plane of the $AR = 2.38$ panel. This behaviour is observed in 7(*a*), which shows that for all cases, Γ_z increases progressively with St. In contrast, beyond $St > 0.6$ of the high-aspect-ratio panel, a peak enhancement in Γ_z at $z = 0$ is observed. Interestingly, at $z = S/2$, the magnitude of Γ_z for both aspect ratio panels approaches zero at large St. This is because of the increased tangled vortices triggered by the gradual enhancements of the spanwise instabilities at higher St values. To show the influence of St on the maximum streamwise vorticity transport leading to changes in circulation, we plot variations of $\Gamma_{x,max}$ with St in figure 7(*b*) for both aspect ratios. We observe that with an increase in St, there is a monotonic increase of $\Gamma_{x,max}$, whereas the peak enhancement is always at $AR = 2.38$. This explains the rapid augmentation in Γ_x with St shown in figure 6(*c,d*). However, for $St \leqslant 0.6$, $\Gamma_{x,max} = 0$, comparable with the maximum Γ_x, which is mostly dominated by the negative values within that regime. Notably, the span of negative Γ_x for $AR = 0.54$ is expanded till $St \leqslant 1$, giving $\Gamma_{x,max} = 0$.

3.3. *Secondary motion*

Secondary motion is the manifestation of the secondary instability, which arises primarily owing to end effects during the pitching motion. For different St, figures 8–9 present streakline visualisations at $y = 0$ (panel (*a–c*)) and $z = 0$ (panel (*d–f*)) planes. For both aspect ratios, we observe a clear indication of the secondary motion from the streaklines. It shows that streaklines from the wide end of the panel start interacting with those of the narrow end slightly downstream of the trailing edge. Notably, the upstream flow displays a weak secondary motion. However, farther downstream of the trailing edge, a rapid spanwise movement of the streaklines, brought about by the higher degree of vortex interactions, causes spanwise compression of the wake width. With an increase in St, the inception of the secondary motion tends to move towards the trailing edge of the panel. It, therefore, triggers its strength, which also makes the wake expand along the panel's normal direction (Buchholz & Smits 2008).

It is to be noted that the combination of pitching motion and end effects promote the onset of 3-D instabilities. We infer from figures 8–9 that for $AR = 0.54$, because the spanwise length is small, such 3-D instabilities can interact with each other, making the
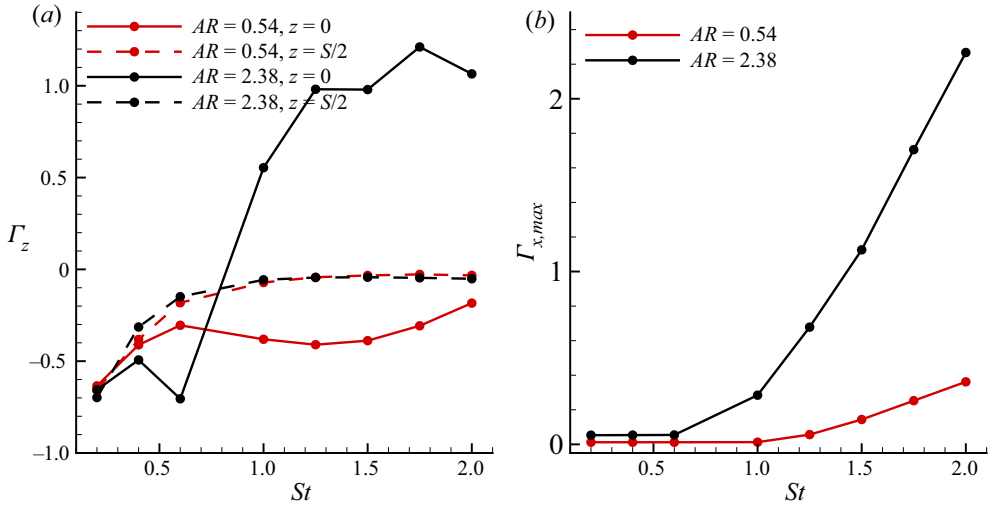
Figure 7. (*a*) The influence of *St* on the dimensionless spanwise circulation for various spanwise locations corresponding to different aspect ratios. (*b*) The effect of *St* on the maximum dimensionless streamwise circulation ($\Gamma_{x,max}$) for different aspect ratios.
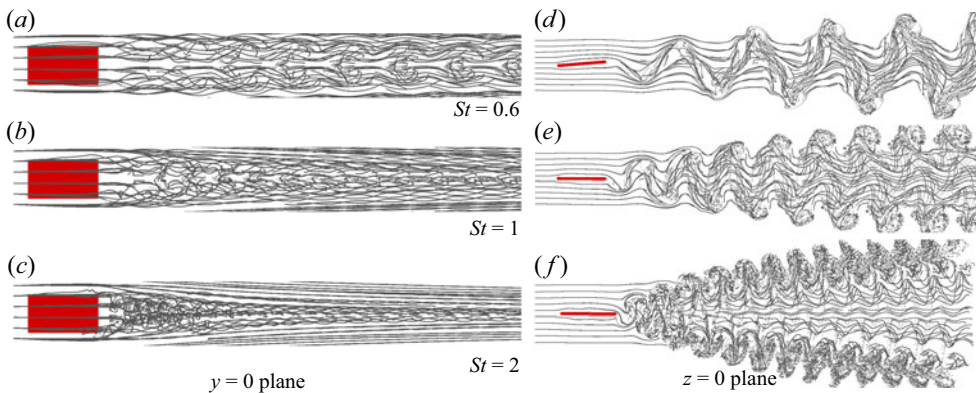

Figure 8. Streakline visualisations of the flow for $AR = 0.54$ and at different *St*. The plan view of the motion is shown in (*a–c*) ($y = 0$ plane), whereas (*d–f*) show an end view of the motion ($z = 0$ plane). The strong secondary motions are noticed from the plan view, which shows progressive wake compression with increase in *St*.

central region less stable. In contrast, the end effects from the two sides hardly reach the central region at $AR = 2.38$. Closer to the central region, flow is nearly two-dimensional (2-D), and only tends to become 3-D when the end effects encroach. Thus, for $AR = 2.38$, we clearly see that near the central region, the flow remains 2-D for smaller *St*. However, because wake compression occurs at higher *St*, the instabilities growing from the two edges spin towards the central region, making it a 3-D flow. Interestingly, a lower value of *St* appears to promote large-wavelength streamwise undulations, which are even more prominent at $AR = 2.38$, while small-scale instabilities are characteristic of an increasing *St*. Thus, the wavelength of the undulations become smaller for increasing *St*, which essentially signifies that high wavenumber disturbances are become more critical at higher *St*.
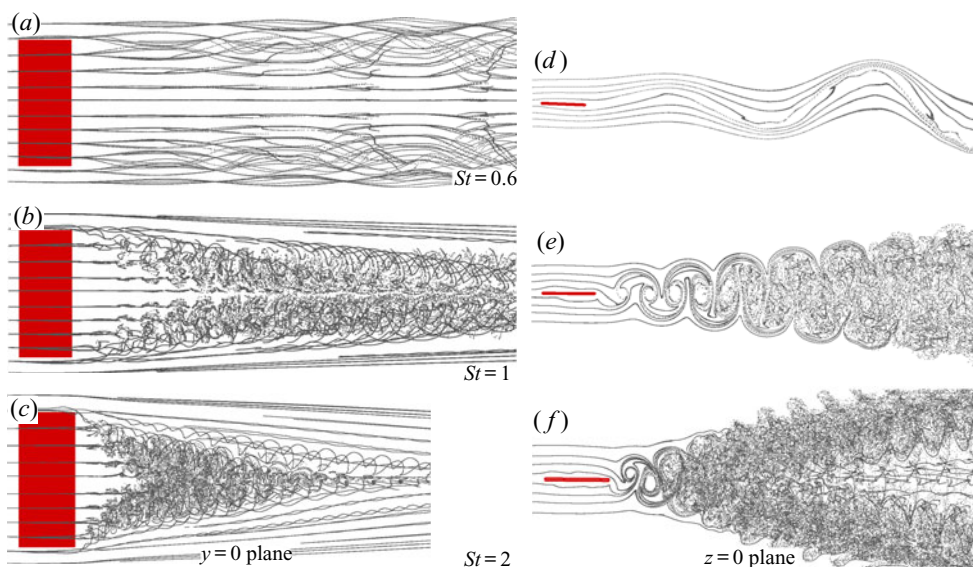
924 A33-15

Figure 9. Streakline visualisations for $AR = 2.38$ and at different St. The plan view of the motion ($y = 0$ plane) is shown in (a–c), whereas (d–f) show an end view ($z = 0$ plane) of the motion.

In the vertical planes of figures 8–9, the top and bottom shear layers diverge. Therefore, the wake width increases with increasing St. The extremities of the shed shear layers form spokes which are symmetrically placed about the central region of the panel. These spokes are seen to become unstable earlier than the rest of the flow and are more explicit at higher St. For large the aspect ratio the flow behaves strangely at smaller St, where we notice the flow to exhibit clear signs of conventional bluff-body motion, and manifest as the entire wake vibrating with the same global frequency. However, as St increases, a vertical bifurcation of the wake appears, which we have commonly termed as the oblique twin jet-type flow pattern. As we can see, higher values of St result in denser jets. An increase in St leads to a stable central region, and hence, it causes a higher concentration of small-scale wake structures at the jet plane through an effective transport from the central zone. The streaklines show a clear picture of the reverse von Kármán vortex street. We further found that the flow has an apparent similarity at higher St for both aspect ratios, but at lower St, they show entirely different behaviour. It is important to note that the three-dimensionality of the wake structures is local in nature, and is seen more at higher St, where it is observed to be non-uniform across the entire wake width in both spanwise and cross-stream directions. The consequence of this is the localisation of non-uniform 3-D instabilities in both spanwise and cross-stream directions.

In figure 10, we show the time-averaged w contours, where dp/dz is overlaid to obtain a possible relationship between them. It is apparent from the figure that the intensity of secondary motion increases with St. The spanwise velocity does not change significantly, even at moderate St and is only seen to increase rapidly at very high values of St. In contrast, dp/dz does not change significantly with St. As we can see, the maximum magnitude $(dp/dz)_{max}$ remains relatively constant. At $AR = 2.38$, while the maximum spanwise velocity almost doubles at $St = 2$, an only marginal increase in the dp/dz is found to come about. Although we observe both favourable and adverse pressure gradients on either side of the central plane in the spanwise direction, the character
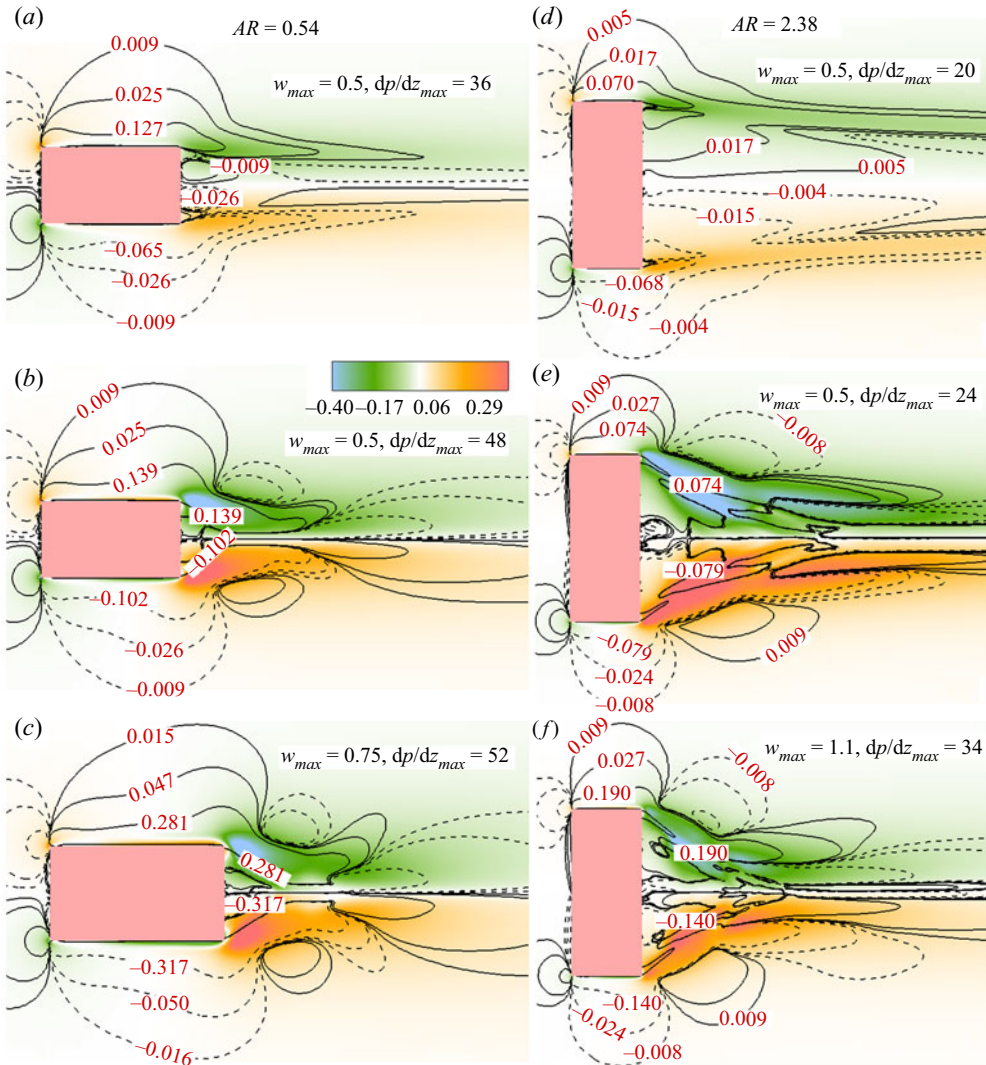
924 A33-16

Figure 10. Isocontour lines of time-averaged spanwise pressure gradient (dp/dz) superimposed on the colour map of the time-averaged spanwise velocity for (*a*) $St = 0.6$, (*b*) $St = 1.5$, (*c*) $St = 2.0$ for $AR = 0.54$ and (*d*) $St = 0.6$, (*e*) $St = 1.5$, (*f*) $St = 2.0$ for $AR = 2.38$.

of the secondary motion shows a symmetric distribution. This, perhaps, indicates that the growth of secondary motion cannot be directly connected to dp/dz; note that large dp/dz and a high-intensity w are seen to coexist locally in the near-wake region, and the two-dimensionality of the flow is again supported by very low-intensity w magnitudes near the central region of the panel. The negatively correlated secondary motion on either side of the central zone re-emphasises strong wake compression at higher St. The pressure gradients are seen to be relatively smooth, even near the edge of the panels, which does not indicate a direct relationship between the secondary instability and the pressure gradient existing locally. Thus, the growth of the secondary instabilities has a greater connection to the intrinsic instabilities than the spanwise pressure gradients.

In figure 11, we plot the streamwise and spanwise distributions of time-averaged spanwise velocity $\langle w \rangle$ as a function of St for different aspect ratios. As evident from frames 11(*a,c*), the intensity of the secondary motion increases several times with increasing St, with a nearly discontinuous jump at the trailing edge of the panel. This trend is attributable to the high cross-stream velocity at the trailing edge, where the radius of motion is maximum. At $St = 2$, such behaviour leads to a larger spanwise velocity, which is seen to be nearly discontinuous. However, at lower values of St, the intensity of the spanwise velocity is far lower. In a time-averaged sense, the nature of the spanwise velocity does not change appreciably at the higher aspect ratio; only the intensity of the flow increases marginally. However, in the spanwise direction, we observe from frames 11(*b,d*) that $\langle w \rangle$ increases dramatically. At higher St, as the wake compression occurs, the maximum spanwise velocity front moves towards the central region of the panel. This event is reflected in the $\langle w \rangle - z$ plot. We observe that the maximum spanwise velocity peak approaches closer to the spanwise direction for increasing St and marginally reaches the central plane. A similar phenomenon is repeated at $AR = 2.38$. However, in the near wake ($x = 1.5$), the magnitude of maximum spanwise velocity for $AR = 2.38$ is nearly four times that of $AR = 0.54$. In the far wake ($x = 5$), it even increases by approximately 10 times. Therefore, we conclude that the growth of secondary motion in the streamwise and spanwise directions does not obey an analogous route. In the streamwise direction, it follows the maximum magnitude. Whereas, in the spanwise direction, the magnitude is several times higher, from smaller to higher aspect ratios. We found that the organisation of the far wake is lost owing to the formations of tangled vortices. This is clear from frame (*d*), where it is seen that the highest velocity does not appear at the highest St. Whereas, at the lower aspect ratio (frame (*b*)), all the spanwise velocities nearly converge. Hence, the spanwise motion decays faster at the smaller-aspect-ratio panel. Interestingly, the secondary motion peaks near the edge of the $AR = 0.54$ panel. In contrast, for $AR = 2.38$, it decays significantly by the time it reaches the edge of the panel. Therefore, the decay in spanwise velocity only starts beyond the edge of the $AR = 0.54$ panel. By comparison, decay starts within the width of the panel for $AR = 2.38$. This also indicates the tendency of increased wake compression at higher aspect ratios.

In frames 11(*a,c*), we observe that for $x > 1$, the flow moves in the positive z direction. Because $\langle w \rangle_{x>1} > 0$ at $z = -S/2$, this clearly signifies a positive z directional motion of the fluid as a consequence of the spanwise wake compression. In contrast, the flow shows completely different behaviour near to the edge of the panel at $x < 1$, where we notice $\langle w \rangle_{x<1} < 0$. Thus, the fluid is diverging away from the panel. We analyse this behaviour in a situation when the momentum of the panel is imparted to the fluid during its pitching motion. As the momentum of the panel is very high, it pushes the fluid away. However, beyond the panel, the fluid approaches the central region because of wake compression. Thus, up to the trailing edge, it deflects the fluid outwards because of the high momentum of the panel. While beyond the trailing edge, because of wake compression, fluid rushes towards the central region. In other words, fluid first displaces and then again reverts to its original location. Such outboard motion induced above the panel is simply a consequence of conservation of mass. We note that the outboard motion of the fluid is nearly 50 %–60 % of the inward motion.

3.4. *Frequency spectrum and space–time behaviour*

We analyse the spreading and timing of the frequency spectra by carrying out a continuous wavelet transform (CWT) of the cross-stream velocity signals at sampling locations,
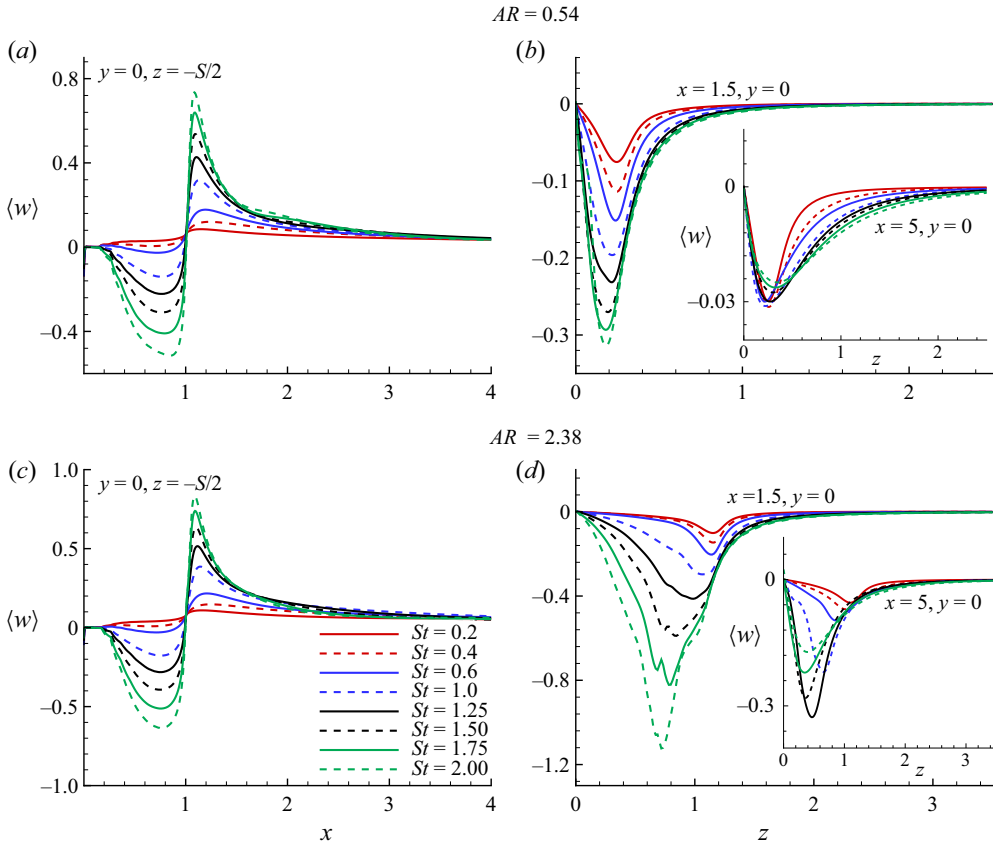
Figure 11. Time-averaged spanwise velocity ($\langle w \rangle$) distribution in the streamwise direction (x) for different St and at a spanwise location of $y = 0$, $z = -S/2$ (a,c). Time-averaged spanwise velocity ($\langle w \rangle$) distribution in the spanwise direction (z) for different St and at a streamwise location of $x = 1.5$, $y = 0$; the inset shows values at $x = 5$, $y = 0$ (b,d). The top and bottom figures show results for $AR = 0.54$ and 2.38.

$(2C, 0, 0)$ and $(2C, -y_{max}, 0)$. In CWT, the coefficient c is generated with position (τ) and scaling argument (s) as, $c(s, \tau) = (1/\sqrt{|s|}) \int_{-\infty}^{\infty} f(t) \overline{\psi}(t - \tau)/s \, \mathrm{d}t$. Where, $\overline{\psi}$ is the complex conjugate of the mother wavelet $\psi(t) = \mathrm{e}^{-t^2/2} \cos 5t$ and $f(t)$ is the pseudo-frequency (De & Sarkar 2020a,b).

The unsteady frequency distribution coloured by the normalised coefficient is shown in figures 12–13 for various St and aspect ratio. The source time-series data are also shown above the CWT map. Depending upon the magnitude of St, the shedding mode is observed to expand from a localised low-frequency to high-frequency mode. In figure 12, we notice that at $St = 0.2$, the entire frequency spectra is dominated by the lower frequency modes and are synchronous with the pitching motion of the panel. Similar behaviour is noted for a higher aspect-ratio panel. However, a narrow band of slightly higher frequency modes is also apparent, but their strength is less than the primary modes. Thus, it has a negligible impact on the overall shedding characteristics. At $St = 0.6$, the increased width of the high-frequency band takes larger values by shifting farther away from the primary lower-frequency band at $AR = 0.54$. In contrast, at $AR = 2.38$, apart from the high-frequency secondary spectrum, intermittent wavelet structures of a larger
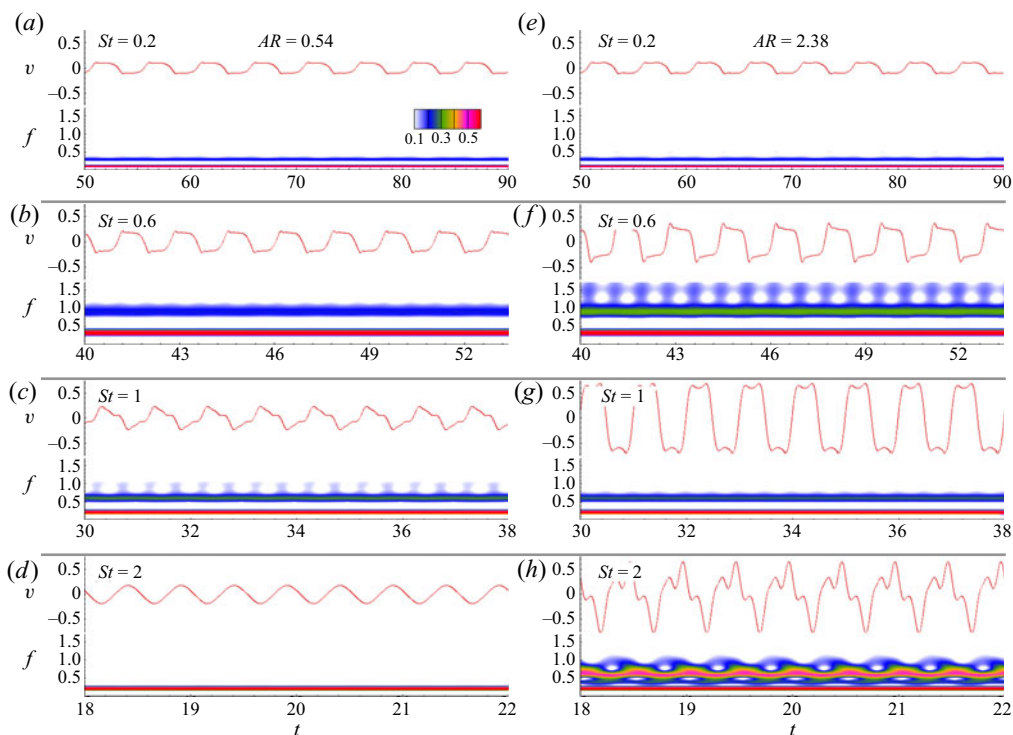
Figure 12. The CWT of the y−velocity signals (v) at a sampling location of $(2C, 0, 0)$. For the various St, CWT results are shown at $AR = 0.54$ (*a–d*) and $AR = 2.38$ (*e–h*) with each panel containing the source time series and CWT map. The colour map of the coefficients normalised by the global maximum is shown in the time-pseudo-frequency domain, $t - f$, depicting the influence of St on the localised frequency concentration.

frequency tertiary spectrum are distributed over the entire period. At $St = 1$, along with the thin band of low-frequency spectrum, lower aspect ratio also exhibits a secondary high-frequency spectrum distributed over a larger bandwidth. An analogous spectrum is apparent for $AR = 2.38$ as well; although, the secondary spectrum has reduced bandwidth. We see that at $St = 2$, a band of low-frequency spectrum thoroughly dominates over the entire period for $AR = 0.54$. Therefore, indicating the complete periodicity of the vortex shedding synchronised with the St of the motion. Whereas, for $AR = 2.38$, along with the dominating low-frequency spectrum, a shallow band of low- to high-frequency wavelet structure is observed.

The CWT results in figure 13 shows St to be dependent on the multi-modal frequency signature. We observe a family of multiple high-frequency spectra at $St = 0.2$ with the band splitting of the spectrum at larger frequency levels. Thus, indicating lateral diffusion of multiple low-frequency cells in the transverse direction. At $St = 0.6$, along with the lower frequency cells, we see a family of multiple large-frequency spectra distributed over oscillating bandwidths at $AR = 0.54$. The peaks of the oscillating bandwidths stretch farther at the higher frequency modes for $AR = 2.38$, yielding wavelet structures related to the localised change in the shedding frequencies. At $St = 1$, the spectral characteristics of the higher-aspect-ratio panel for both of the sampling locations show similar behaviour. In contrast, at $AR = 0.54$, we notice a broader spread of the wavelet structure at the larger-frequency spectrum ranging from the lower-frequency regime to
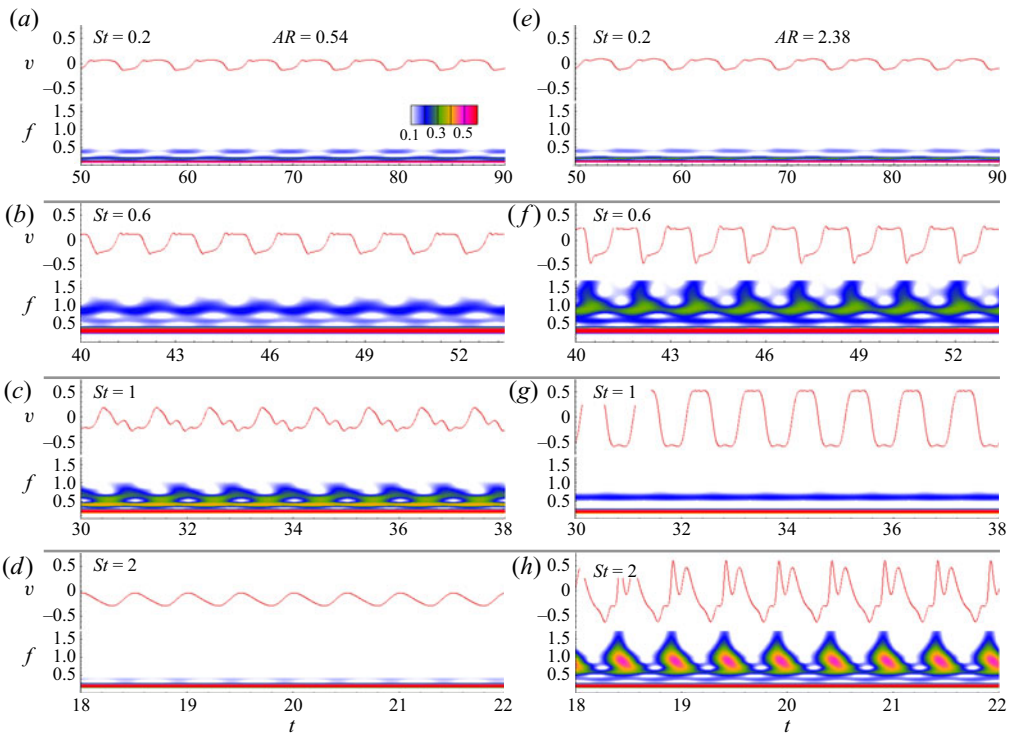
924 A33-20

Figure 13. The CWT of the cross-stream velocity signals (v) at a sampling location of $(2C, -y_{max}, 0)$. For various St, CWT results are shown at $AR = 0.54$ (a–d) and $AR = 2.38$ (e–h) with each panel containing the source time series and CWT map. The colour map of the coefficients normalised by the global maximum is shown in the time-pseudo-frequency domain, $t - f$, depicting the influence of St on the localised frequency concentration.

higher-frequency spikes. Such behaviour is attributable to the bifurcating wake structures observed at this Strouhal number value. At $St = 2$, the entire spectrum for $AR = 0.54$ is dominated by the low-frequency shedding modes locked in with the pitching motion. We observe the frequency spectrum having a flame-type wavelet structure distributed throughout the entire temporal domain for $AR = 2.38$. Notably, the core of the flame shows an equal strength synchronised frequency surrounded by the larger-frequency spectrum.

Figure 14 depicts the spatio–temporal response of v at a section $y = A/2$ on the $z = 0$ plane in the streamwise direction for five shedding cycles. If we draw a horizontal line at a specified time, it intersects the wake at positive and negative values in an alternative manner. This clearly suggests highly coherent and periodic patterns of vortex structures across the streamwise extremes. We found a constant time lag between the shed vortices for a given St. An increase in St generates additional time lags, and the maximum is noticed at $St = 2$. Remarkably, the periodic vortex structures on the panel extent do not follow the St dependence of the time lag, which starts beyond the trailing edge ($x > 1$) and end at the downstream wake. For $St = 0.2$ and 0.6, a broadening of the cells is evident, indicating the growth of large-scale deformations associated with a vortex core flattening, this eventually imparts a stabilising influence on the near wake. In contrast, we observe streamwise diffusion of the cells for $St > 1$. At $St = 2$, we see that for $AR = 0.54$, vortex structures mark their presence up to a location of $x \approx 3$. Beyond $x > 3$, there is hardly any appearance
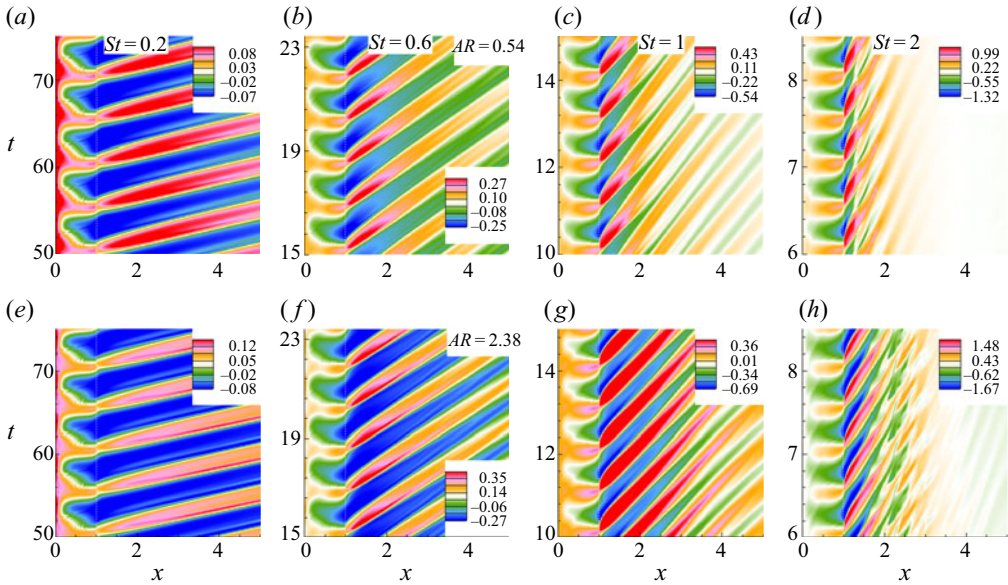
Figure 14. Space–time reconstruction of the vertical velocity (v) in the streamwise direction at a vertical section $y = A/2$ on the midspan plane $z = 0$. Note that while the x-axis represents the streamwise direction, the time evolution is displayed in the y direction.

of vertical velocities and, therefore, the corresponding absence of the wake vortices. This behaviour is attributed to the bifurcations of the primary vortex into a pair of transversely oriented twin-jet-type vortex trajectories. At $AR = 2.38$, we observe a similar behaviour with an intermittent impression of high-frequency cells beyond $x > 3$. This is attributable to the presence of multiple bifurcated structures comprising of swirling rings of vortices at $St = 2$. Eventually, as the vortex structure becomes increasingly irregular with the downstream distance from the trailing edge, we observe the emergence of temporally correlated multiple velocity spots within the spatial regime $2 \leqslant x \leqslant 3$.

Along the span, figure 15 shows the temporal evolution of w velocity at a downstream section $x = 1.5$ on $y = 0$ plane for five vortex shedding cycles. We observe that the time-periodic negative and positive vortical structures symmetrically spanning across the positive and negative extremities of the panel about the $z = 0$ plane. The core of the structures is positioned near the end of the panel, where the area occupied by the temporally correlated cells is more prevalent for $AR = 0.54$. With increasing St, the growth of the secondary motion causes the spanwise cells to advance towards the central plane. Such narrowing down of the cells clearly highlights the signature of the wake compression. We further notice that structures are highly concentrated at the central plane for $AR = 0.54$ at $St = 2$ which show a periodic behaviour. At $AR = 2.38$, we observe the formation of primary and secondary highly concentrated periodic cells restrained within a narrow band on either side of the central plane. Interestingly, we notice the occurrence of period doubling on the spanwise cells. Irrespective of St and aspect ratio, the space–time reconstruction results of the streamwise cells in figure 14 shows five periods in as many shedding cycles. In contrast, the corresponding behaviour for the spanwise cells in figure 15 yield a doubling of the periods. To our knowledge, this period-doubling behaviour of the spanwise cells is probably the first demonstration for low-aspect-ratio pitching panels. We attribute this period-doubled response of the spanwise cells to the
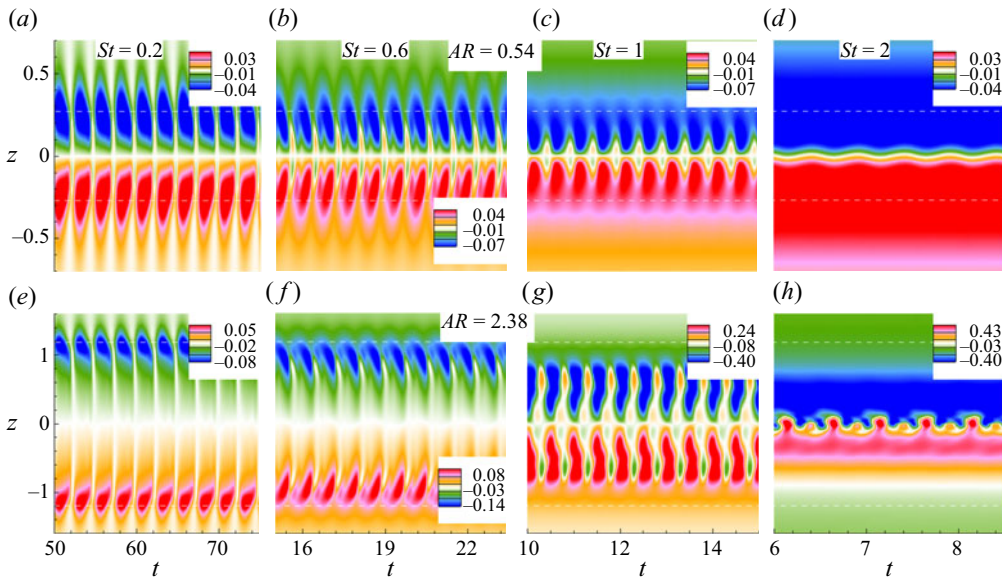
Figure 15. Space–time reconstruction of the spanwise velocity (w) along the span at a downstream section $x = 1.5$ on the mid-vertical plane $y = 0$. Note that while the y-axis represents the span, the time evolution is displayed in the x direction.

periodic formation of moderately distorted spanwise vortex structures and more complex structures characterised by the vortex rollup of inclined helical structures.

3.5. *Wake vortex interactions*

Figure 16 shows the streamwise interactions of the vortices through instantaneous ω_z contours located at the $z = 0$ plane for various St and aspect ratio. We observe that for increasing St, vortical structures show two transitions with three independently distinct wake patterns. In the regime, $0.2 \leqslant St \leqslant 0.6$, a pair of oscillating shear layers emerged from the panel with the tip connecting the leading edge, which roll up into horseshoe and bow-shaped vortices for $AR = 0.54$ and $AR = 2.38$, respectively. The wake does not resemble any discrete vortex structures from the side, usually characterised by elongated strands of negative and positive vorticity. The flow constricts downstream of the trailing edge, producing a wake with an appearance of diffused packets of negative and positive vortex contrails. The formation length of the vortex contrail decreases with increasing St, and the wake shows more dense diffused structures.

For $St = 1$, the wake shows a clear signature of a reverse von Kármán vortex street for both aspect ratios. The longitudinal diffusion between the wake structures is less for $AR = 0.54$. This signifies minimal interactions between the cross-stream vorticities as attributed to the chain of engulfed horseshoe vortex structures. As such, each horseshoe vortex constitutes combinations of closed-loop vortices bound together at the tip with branching out the legs that distribute along the length to evolve into a spanwise shear layer (Buchholz & Smits 2008). As a result, the self-induction of the curved tips causes transverse wake expansion farther downstream. At $AR = 2.38$, the shed vortices from the trailing edge maintain a clear pattern, displaying a periodic flow field up to $2C$ downstream length. Thereafter, it bifurcates into multiple alternately signed streamwise
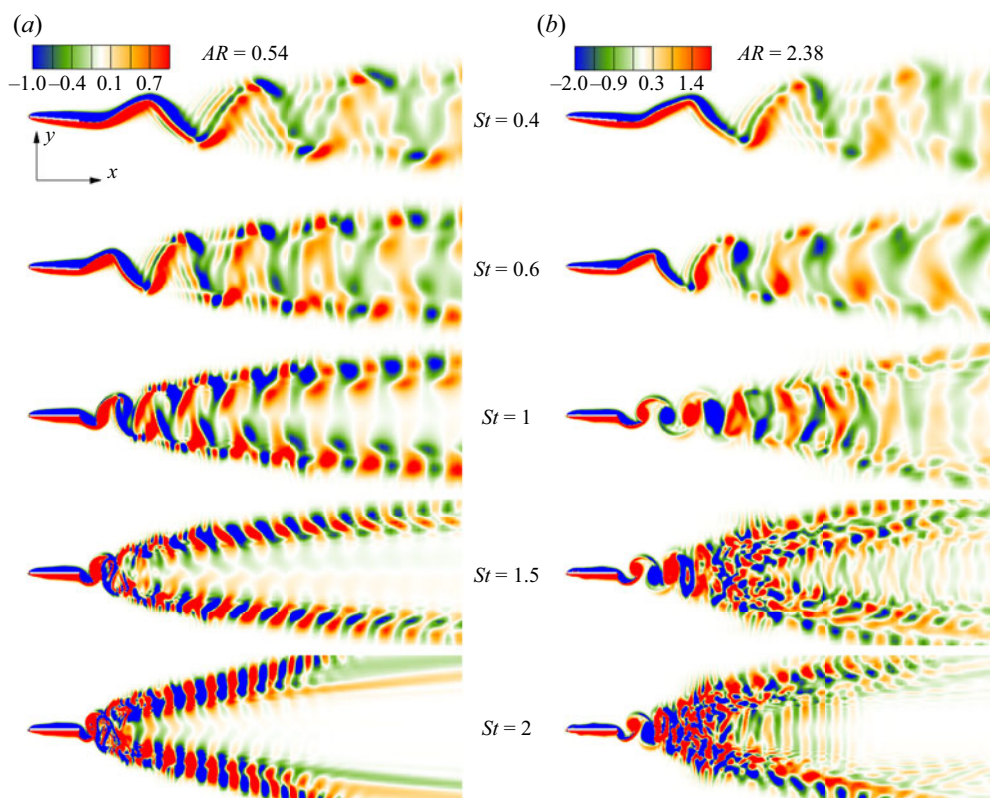
Figure 16. Instantaneous 2-D vorticity contours in the *x*–*y* plane (ω_z) for different Strouhal numbers; (*a*) corresponds to $AR = 0.54$ and (*b*) corresponds to $AR = 2.38$.

cells, resulting in a transverse wake expansion. It is to be noted that the transverse expansion is associated with spanwise wake compression owing to the mutual induction of counter-signed streamwise vortex pairs both at the bottom and top of the wake (Buchholz & Smits 2008). Farther downstream, these streamwise cells undergo lateral diffusion to yield blurred wake patterns.

The wake splits for $St \geqslant 1.25$, developing two independent jets of vortex structures. There, the mean wake is symmetrically placed about the wake centreline. The corresponding structures, constituting each train, resemble coherent cells of consecutive positive and negative vortex loops. The strength and orientation of the loops change with *St*. At $St = 1.5$ and 2, we observe an approximately 45° phase difference between the structures, with respect to the axis of the panel. Interestingly, the angle between the bifurcated streamwise jets increases with increasing *St* and results in an expansion of the wake width. A larger wake width leads to a stable central region, which opposes any interaction between the streamwise or cross-stream vortices. In contrast, at $AR = 2.38$, a more complex flow structure is observed. The bifurcated wake constitutes randomly distributed complex vortex loops and vortex contrails interacting with each other. The complexities in the flow field are further aggravated by increasing the Strouhal number. At $St = 2$, approximately $C/2$ downstream from the trailing edge, appearances of distorted vortex loops and entangled structures augmenting both streamwise and cross-stream interactions of the vortices are seen.
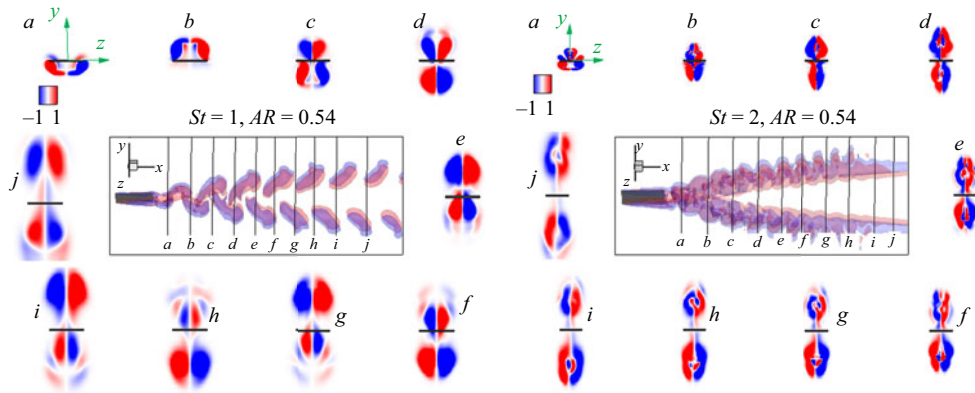
924 A33-24

Figure 17. Instantaneous planar view of streamwise vorticity contours (ω_x) at various transverse planes (y–z) at $AR = 0.54$ for $St = 1$ (left panel) and $St = 2$ (right panel). Interactions between vortices shown at cross-sectional planes (a–j) designate $1.2 \leqslant x/C \leqslant 5.5$ with $\Delta x/C \approx 0.4$.

We analysed the vortex interactions with the instantaneous ω_x contours at various transverse planes within the wake. Figure 17 shows that at $St = 1$, plane a, which is located near to the trailing edge, contains counter-rotating pairs of the immediately shed horseshoe legs. Plane (b) contains the tip of the horseshoe connected to plane (a), which grows in size and strength with downstream distance. The interactions between the top and bottom horseshoes shed in the successive previous half cycles are seen in planes (c–e). We see leapfrog type interactions between the counter-rotating vortex pairs about the planes (c–e) (Buchholz & Smits 2006). The plane (f) contains the tip of the lowest horseshoe associated with plane (e) and leg of the top horseshoe shed in the previous half period. The interaction pattern is similar to the one observed for planes (c–e). We notice similar repeated patterns in planes (g–j), where the vortices shed earlier than those in planes (c–f) for the consecutive four half-cycles. Notably, the distance between the cores of top and bottom vortex loops increases with increasing downstream distance from the trailing edge, resulting in weak cross-stream interactions. In contrast, the vortex interactions at $St = 2$ shows merging and dissipation of vortex loops at various sectional planes (a–j). Plane (a), lying at the jet bifurcation zone, shows mutual interactions between the two most recently shed, oppositely oriented, tip and leg of the hairpin-like vortex structures. Plane (b) contains bifurcated structures, where vortices are seen to shed one pitching cycle earlier than those of plane (a). We observe vertical stretching of the vortex loops with increased strength and surface area. Additionally, there is spanwise merging of the cores at the symmetry axis ($z = 0$). In the subsequent planes (c–j), the vortex pairs grow in size with the merging of the core, leading to the emergence of secondary core-split structures.

At $St = 1$ in figure 18, plane (a), near to the trailing edge shows the legs of immediately shed bow-shaped vortices. Plane (b) carries counter-signed vorticity loops consisting of the leg of the top vortex shed at the previous half-cycle and the tips of the immediately shed vortices. The complexities of the vortex interactions in the successive downstream planes (c–j) increase because of the complexities of the flow field. Again, owing to rapid cross-stream momentum exchange, the vortical loops across planes (c–j) undergo vortex merging, which increases with the downstream distance from the trailing edge. As a result, we observe the formation of vortex contrails of alternating sign. This is further exacerbated under the influence of the secondary instabilities. The evolution of new vortex
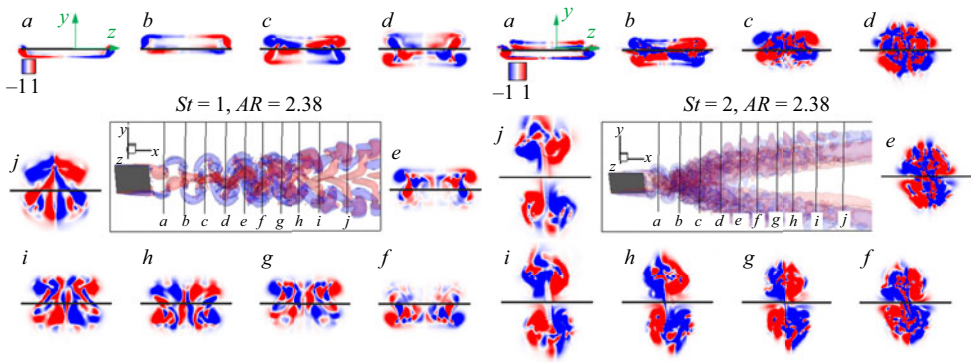
Figure 18. Planar view of instantaneous streamwise vorticity contours (ω_x) at various transverse planes at $AR = 2.38$ for $St = 1$ (left panel) and $St = 2$ (right panel). Vortex interactions are shown at cross-sectional planes (a–j) designate $1.2 \leqslant x/C \leqslant 5.5$ with $\Delta x/C \approx 0.4$.

couples and also the ensuing merging process is recurrent in planes (g–j). We observe from planes (a–j) that the structures have reflection symmetry about the $z = 0$ plane marked by counter-rotating positive and negative vortex loops. Moreover, the maximum circulation strength is seen for the furthest plane (j) with fewer cells covering the maximum area. In comparison, an alternate sign of chaotic structures spanning across the y–z plane is seen at $St = 2$. Apart from plane (a), containing the leg of the instantly shed vortex, we cannot make any quantifiable information regarding primary vortex interaction patterns from planes (b–j). We notice accelerated cross-stream meandering interactions between multiple vortex loops for the downstream planes (b–f). For the planes (g–j), bifurcation in the wake disrupts cross-stream vorticity interactions and triggers localised interactions between the vorticity loops. It is possible that we see the formation of bridgelet-type vortex contrail connecting top and bottom vortices, located symmetrically about the plane $y = 0$.

3.6. *Force coefficients*

In figure 19, we show the time histories of C_T and C_L for different St. In the right-hand panel, we show $C_T - C_L$ phase portraits for each St and aspect ratio. This reveals that both C_T and C_L signals display a constant amplitude regular oscillations for the entire range of St. This essentially indicates periodic dynamics during the pitching motion. The panel experiences maximum thrust force just before it reaches pitching extremes and we notice that C_T attains two peaks for all St values. We find that the magnitude of C_L is nearly twice that of C_T (Dong *et al.* 2006; Dai *et al.* 2012). We attribute this observation to the larger amplitude of forced oscillations that exhibit stronger circulation in the shed vortices. It is found that the $C_T - C_L$ phase portraits reveal a closed attractor representing the periodic signature of the pitching motion. The phase portraits take the standard '8'-shaped loop where the crossover point is always located at $C_L = 0$. Interestingly, for both aspect ratios, increasing St leads to the gradual movement of the crossover point towards the positive C_T axis, thereby causing the phase portrait to undergo a flip-flop transition. At $St \geqslant 1$, the crossover point ceases its movement, and the phase portrait resembles a mirror-image symmetry similar to the one for $St = 0.2$. For all St, there is a significant enhancement in the force coefficients with an increase in aspect ratio.

In figure 20(*a*), we plot the variation in the mean thrust ($\overline{C_T}$), lift ($\overline{C_L}$) and spanwise force ($\overline{C_Z}$) coefficients as a function St for $AR = 0.54, 2.38$. We note that $\overline{C_T}$ increases
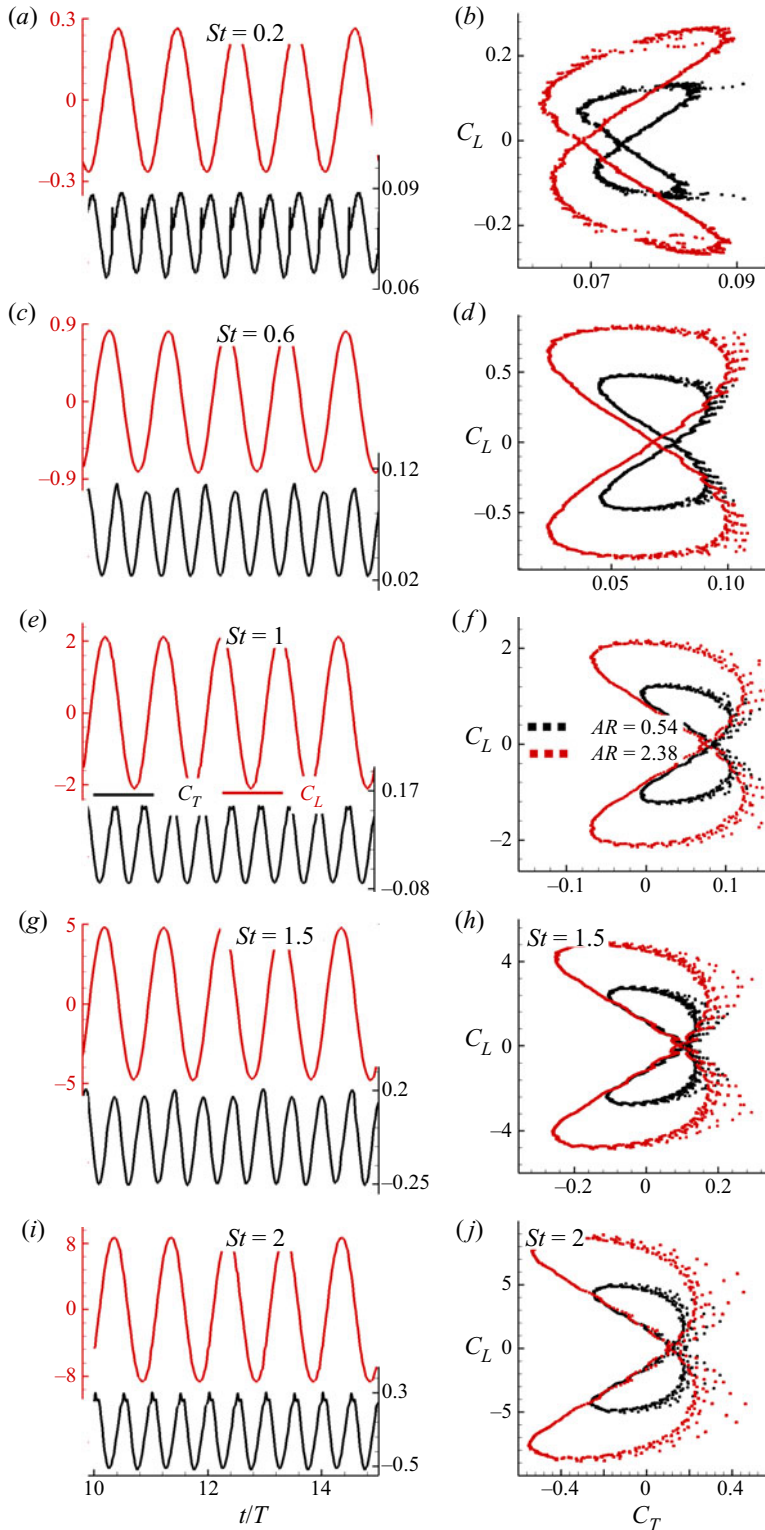
Figure 19. Time histories of the thrust (C_T) and lift (C_L) coefficients for different Strouhal numbers, where $T = St^{-1}$. The corresponding $C_T - C_L$ phase portraits are shown in the right-hand panel.
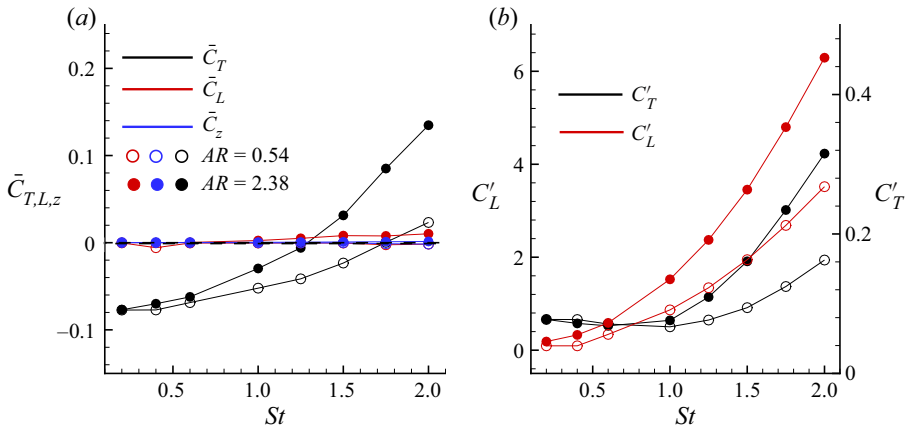
Figure 20. (a) Coefficient of mean thrust ($\overline{C_T}$), mean lift ($\overline{C_L}$) and spanwise mean force coefficient ($\overline{C_Z}$) as a function of St for different aspect ratios. (b) Variations of the r.m.s. thrust (C_T') and lift (C_L') coefficients with the Strouhal number for $AR = 0.54$, 2.38, respectively.

monotonically with St, and that $\overline{C_T}$ is higher for larger aspect ratio, yielding a steeper $\overline{C_T} - St$ curve. We observe that a regime of negative $\overline{C_T}$ prevails for $St \lesssim 1.2$ at $AR = 2.38$, whereas the corresponding region at $AR = 0.54$ is $St \lesssim 1.7$. The streaming speed is the strong influencing parameter to yield negative $\overline{C_T}$ for these St regimes, which becomes higher than the thrust produced by the panel. The results of negative $\overline{C_T}$ bear resemblance with the experimental results of Fernandez-Prats (2017) for a square rigid pitching panel. Moreover, the point of $\overline{C_T} = 0$, indicating a symmetric C_T signal about the $C_T = 0$ axis, occurs at higher St for decreasing aspect ratio. We found the zero mean thrust free-pitching condition for $(St)_{AR=0.54} \approx 1.75$ and $(St)_{AR=2.38} \approx 1.32$. Figure 20(a) also depicts that changes in $\overline{C_L}$ are insignificant with increasing St, and their values, although finite, are close to zero. This again demonstrates the symmetric nature of C_L time signals for all St. For the present range of St, our computations show $F_z = 0$, therefore, yielding $\overline{C_Z} = 0$.

In figure 20(b), we show the variations of root-mean-squared (r.m.s.) thrust (C_T') and lift (C_L') coefficients with St for $AR = 0.54$, 2.38. The plot shows that both C_T' and C_L' increase with St and aspect ratio, reaching a peak at $St = 2$. We found that C_L' increases significantly with St, although $\overline{C_L} \approx 0$. However, the magnitudes of C_T' are significantly smaller ($O(10^{-1})$) in contrast to C_L' ($O(10)$). These enhancements in C_L' are attributed to the increased relative strengths of the horseshoe vortices and subsequent formations of the bifurcated jets at larger St. Furthermore, at $AR = 2.38$, increasing St causes the formation of multiple vortex contrails and a complex flow structure. The overall effect is a trigger in flow fluctuations and thereby increased magnitudes of C_L'.

4. Conclusions

We performed numerical simulations of flow past a thin pitching panel of aspect ratio 0.54 and 2.38 placed in a uniform flow for $Re = 1000$. In particular, we have considered a wide range of $0.2 \leqslant St \leqslant 2$ to analyse the influence of pitching frequency on the 3-D vortex dynamics. Our computations show that within this range of St, the wake transition reveals vortex structures comprising horseshoe vortices at $St = 0.6$, bow-shaped vortices, vortex rings, hairpin vortices at $St = 1.75$, secondary bridgelets and large-tangled 3-D vortex

924 A33-28

structures for $St \geqslant 1.5$. We found a reverse von Kármán vortex street in the near wake for both aspect-ratio panels at $St = 1$. An increase in $St > 1$ reveals wake bifurcation into twin jets. At $AR = 0.54$, the hairpin vortices transform into vortex rings, which start rotating at $St = 2$. On the other hand, transverse asymmetrically bifurcated tangled vortices rolling over the isolated arrays of parallel strips are seen at $AR = 2.38$.

We found that circulation strength increases with St. The influences of aspect ratio and St showed an increased spanwise movement of the flow. The flow converges towards the central region to yield wake compression at larger St. The wake compression is associated with a lower velocity magnitude at the central region than for the side wake. We found that the mechanism of the wake compression is attributable to the secondary instabilities driven by the spanwise pressure gradient, previously triggered by end effects. Streakline visualisations show a progressive growth in the wake width with increasing St. We found the formation of spokes at the shear-layer extremities for higher St, which become unstable earlier than the rest of the flow. The wake resembles a clear signature of conventional bluff-body motion at $AR = 2.38$, resulting in a synchronised flow. Our results revealed the local nature of the three-dimensionality in the wake structures, and such localisation is higher at larger St.

The CWT at the midspan for $AR = 0.54$ at $St = 2$ indicates a low-frequency band across the entire period, indicating periodic flow locked in with the pitching motion. The space–time behaviour in the streamwise direction reveals a constant time lag between the shed vortex structures for increasing St. At $AR = 2.38$, $St = 2$, we found irregular temporally correlated multiple velocity spots within the spatial regime $2 \leqslant x \leqslant 3$. Interestingly, we have revealed the occurrence of period-doubling in the space–time behaviour of the spanwise cells.

The streamwise vortex interactions show that for $St \leqslant 1$, the wake exhibits elongated strands of negative and positive vortices. Far downstream, the wake gives the appearance of diffused packets of negative and positive vortex contrails. The bifurcated jets found at $St \geqslant 1.25$ for $AR = 0.54$ lead to an enhanced wake width, where the angle between the jets is found to increase with St. For $AR = 2.38$, we found a chaotic signature in the wake constituting random interactions of vortex loops and vortex contrails. The $C_T - C_L$ phase portraits are found to behave as a closed attractor, which undergoes flip-flop transition with increasing St. The mean thrust coefficient increases monotonically with St and aspect ratio. The r.m.s. thrust and lift coefficients show enhancement with St and aspect ratio.

Author ORCIDs.
Ⓓ Arnab Kumar De https://orcid.org/0000-0003-4647-954X;
Ⓓ Sandip Sarkar https://orcid.org/0000-0002-4442-5882.

REFERENCES

AGARWAL, A., NOLAN, K.P., STAFFORD, J. & JEFFERS, N. 2017 Visualization of three-dimensional structures shed by an oscillating beam. *J. Fluids Struct.* **70**, 450–463.

ANDERSON, J.M., STREITLIEN, K., BARRETT, D.S. & TRIANTAFYLLOU, M.S. 1998 Oscillating foils of high propulsive efficiency. *J. Fluid Mech.* **360**, 41–72.

BISWAS, G. & SARKAR, S. 2009 Effect of thermal buoyancy on vortex shedding past a circular cylinder in cross-flow at low Reynolds numbers. *Intl J. Heat Mass Transfer* **52**, 1897–1912.

BLONDEAUX, P., FORNARELLI, F., GUGLIELMINI, L., TRIANTAFYLLOU, M.S. & VERZICCO, R. 2005 Numerical experiments on flapping foils mimicking fish-like locomotion. *Phys. Fluids* **17**, 113601.

BORAZJANI, I. & SOTIROPOULOS, F. 2008 Numerical investigation of the hydrodynamics of anguilliform swimming in the transitional and inertial flow regimes. *J. Expl Biol.* **212**, 576–592.

BORAZJANI, I. & SOTIROPOULOS, F. 2009 Vortex-induced vibrations of two cylinders in tandem arrangement in the proximity-wake interference region. *J. Fluid Mech.* **621**, 321–364.

BOSE, C. & SARKAR, S. 2018 Investigating chaotic wake dynamics past a flapping airfoil and the role of vortex interactions behind the chaotic transition. *Phys. Fluids* **30**, 047101.

BUCHHOLZ, J.H.J. 2006 The flow field and performance of a low aspect ratio unsteady propulsor. PhD thesis, Princeton University.

BUCHHOLZ, J.H.J., JIMENEZ, J.M., ALLEN, J.J. & SMITS, A.J. 2003 Hydrodynamics of thrust production in a fish-like flapping membrane. In *13th International Symposium on Unmanned Untethered Submersible Technology. University of New Hampshire, Durham, NH.*

BUCHHOLZ, J.H.J. & SMITS, A.J. 2006 On the evolution of the wake structure produced by a low-aspect-ratio pitching panel. *J. Fluid Mech.* **546**, 433–443.

BUCHHOLZ, J.H.J. & SMITS, A.J. 2008 The wake structure and thrust performance of a rigid low-aspect-ratio pitching panel. *J. Fluid Mech.* **603**, 331–365.

CALDERON, D.E., CLEAVER, D.J., GURSUL, I. & WANG, Z. 2014 On the absence of asymmetric wakes for periodically plunging finite wings. *Phys. Fluids.* **26**, 071907.

CLARK, R.P. & SMITS, A.J. 2006 Thrust production and wake structure of a batoid-inspired oscillating fin. *J. Fluid Mech.* **562**, 415–429.

CLEAVER, D.J., WANG, Z. & GURSUL, I. 2012 Bifurcating flows of plunging aerofoils at high Strouhal numbers. *J. Fluid Mech.* **708**, 349–376.

DAI, H., LUO, H., FERREIRA DE SOUSA, P.J.S.A. & DOYLE, J.F. 2012 Thrust performance of a flexible low-aspect-ratio pitching plate. *Phys. Fluids* **24**, 101903.

DE, A.K. 2016 A diffuse interface immersed boundary method for convective heat and fluid flow. *Intl J. Heat Mass Transfer* **92**, 957–969.

DE, A.K. 2018 A diffuse interface immersed boundary method for complex moving boundary problems. *J. Comput. Phys.* **366**, 226–251.

DE, A.K. & SARKAR, S. 2020*a* Three-dimensional wake dynamics behind a tapered cylinder with large taper ratio. *Phys. Fluids* **32**, 063604.

DE, A.K. & SARKAR, S. 2020*b* Wake events during early three-dimensional transition of a circular cylinder placed in shear flow. *Phys. Fluids* **32**, 053603.

DEWEY, P.A., CARRIOU, A. & SMITS, A.J. 2012 On the relationship between efficiency and wake structure of a batoid-inspired oscillating fin. *J. Fluid Mech.* **691**, 245–266.

DHANAK, M. & BERNARDINIS, B. 1981 The evolution of an elliptic vortex ring. *J. Fluid Mech.* **109**, 189–216.

DONG, H., BOZKURTTAS, M., MITTAL, R., MADDEN, P. & LAUDER, G.V. 2010 Computational modelling and analysis of the hydrodynamics of a highly deformable fish pectoral fin. *J. Fluid Mech.* **645**, 345–373.

DONG, H., MITTAL, R. & NAJJAR, F.M. 2006 Wake topology and hydrodynamic performance of low-aspect-ratio flapping foils. *J. Fluid Mech.* **566**, 309–343.

EBRAHIMI, N.D., ELDREDGE, J.D. & JU, Y.S. 2020 Three-dimensional characteristics of the jet flows induced by a pitching plate in a quiescent fluid. *J. Fluid Mech.* **887**, A25.

VON ELLENRIEDER, K.D., PARKER, K. & SORIA, J. 2003 Flow structures behind a heaving and pitching finite-span wing. *J. Fluid Mech.* **490**, 129–138.

ELLINGTON, C.P. 1984 The aerodynamics of hovering insect flight. II. Morphological parameters. *Phil. Trans. R. Soc. Lond.* B **305**, 17–40.

FERNANDEZ-PRATS, R. 2017 Effect of chordwise flexibility on pitching foil propulsion in a uniform current. *Ocean Engng* **145**, 24–33.

FISH, F., SCHREIBER, C., MOORED, K., LIU, G., DONG, H. & BART-SMITH, H. 2016 Hydrodynamic performance of aquatic flapping: efficiency of underwater flight in the manta. *Aerospace* **3**, 20.

FREYMUTH, P. 1988 Propulsive vortical signature of plunging and pitching airfoils. *AIAA J.* **27** (9), 1200–1205.

FREYMUTH, P., FINAISH, F. & BANK, W. 1987 Further visualization of combined wing tip and starting vortex systems. *AIAA J.* **25** (9), 1153–1159.

GHOVARDHAN, R. & WILLIAMSON, C.H.K. 2005 Vortex-induced vibrations of a sphere. *J. Fluid Mech.* **531**, 11–47.

GREEN, M.A. & SMITS, A.J. 2008 Effects of three-dimensionality on thrust production by a pitching panel. *J. Fluid Mech.* **615**, 211–220.

GUGLIELMINI, L. 2004 Modeling of thrust generating foils. PhD thesis, University of Genoa.

HEMMATI, A., VAN BUREN, T. & SMITS, A.J. 2019 Effects of trailing edge shape on vortex formation by pitching panels of small aspect ratio. *Phys. Rev. Fluids* **4**, 033101.

HULTMARK, M., LEFTWICH, M. & SMITS, A.J. 2007 Flowfield measurements in the wake of a robotic lamprey. *Exp. Fluids* **43**, 683–690.

JAFARI, P., MASOUDI, A., IRAJIZAD, P., NAZARI, M., KASHYAP, V., ESLAMI, B. & GHASEMI, H. 2018 Evaporation mass flux: a predictive model and experiments. *Langmuir* **34** (39), 11676–11684.

JEONG, J. & HUSSAIN, F. 1995 On the identification of a vortex. *J. Fluid Mech.* **285**, 69–94.

KIM, D., STROM, B., MANDRE, S. & BREUER, K. 2017 Energy harvesting performance and flow structure of an oscillating hydrofoil with finite span. *J. Fluids Struct.* **70**, 314–326.

KOOCHESFAHANI, M.M. 1989 Vortical patterns in the wake of an oscillating airfoil. *AIAA J.* **27**, 1200–1205.

KUSHWAHA, V.K.. & DE, A.K. 2020 Aerodynamics of multiple freely falling plates. *Phys. Fluids* **32**, 103603.

LI, C. & DONG, H. 2016 Three-dimensional wake topology and propulsive performance of low-aspect-ratio pitching-rolling plates. *Phys. Fluids* **28**, 071901.

LI, G.-J. & LU, X.-Y. 2012 Force and power of flapping plates in a fluid. *J. Fluid Mech.* **712**, 598–613.

LIANG, Z. & DONG, H. 2015 On the symmetry of proper orthogonal decomposition modes of a low-aspect-ratio plate. *Phys. Fluids* **27**, 063601.

NAZARI, M., MASOUDI, A., JAFARI, P., IRAJIZAD, P., KASHYAP, V. & GHASEMI, H. 2018 Ultrahigh evaporative heat fluxes in nanoconfined geometries. *Langmuir* **35** (1), 78–85.

OSHIMA, Y. & NATSUME, A. 1980 Flow field around an oscillating airfoil. In *Flow Visualization II. Proceedings Second International Symposium on Flow Visualization, Bochum, W. Germany* (ed. W. Merzkirch). Hemisphere.

OSHIMA, Y. & OSHIMA, K. 1980 Vortical flow behind an oscillating airfoil. In *Proceedings 15th Congress, International Union of Theoretical and Applied Mechanics*. North Holland.

PAN, D. & SHEN, T.T. 2009 Computation of incompressible flows with immersed bodies by a simple ghost cell method. *Intl J. Numer. Meth. Fluids* **60**, 1378–1401.

PANAH, A.E., AKKALA, J.M. & BUCHHOLZ, J.H.J. 2013 Vortex dynamics of a finite-aspect-ratio plunging wing. In *51st AIAA Aerospace Sciences Meeting including the New Horizons Forum and Aerospace Exposition 2013 – Grapevine, TX, United States*. AIAA.

PRINCE, C., LIN, W., LIN, J., PETERSON, S.D. & PORFIRI, M. 2010 Temporally-resolved hydrodynamics in the vicinity of a vibrating ionic polymer metal composite. *J. Appl. Phys.* **107** (9), 094908.

RICHARD, B. 1958 The speed of swimming of fish as related to size and to the frequency and amplitude of the tail beat. *J. Expl Biol.* **35**, 109–133.

RINGUETTE, M.J., MILANO, M. & GHARIB, M. 2007 Role of the tip vortex in the force generation of low-aspect-ratio normal flat plates. *J. Fluid Mech.* **581**, 453–468.

SARKAR, S. & VENKATRAMAN, K. 2006 Numerical simulation of thrust generating flow past a pitching airfoil. *Comput. Fluids* **35**, 16–42.

TAIRA, K. & COLONIUS, T. 2009 Three-dimensional flows around low-aspect-ratio flat-plate wings at low Reynolds numbers. *J. Fluid Mech.* **623**, 187–207.

TAYLOR, G., NUDDS, R. & THOMAS, A. 2003 Flying and swimming animals cruise at a Strouhal number tuned for high power efficiency. *Nature* **425**, 707–711.

THEKKETHIL, N., SHARMA, A. & AGRAWAL, A. 2020 Three-dimensional biological hydrodynamics study on various types of batoid fishlike locomotion. *Phys. Rev. Fluids* **5**, 023101.

TORRES, G.E. & MUELLER, T.J. 2004 Low-aspect-ratio wing aerodynamics at low Reynolds numbers. *AIAA J.* **42** (5), 865–873.

TRIANTAFYLLOU, G.S., TRIANTAFYLLOU, M.S. & GROSENBAUGH, M.A. 1993 Optimal thrust development in oscillating foils with application to fish propulsion. *J. Fluids Struct.* **7**, 205–224.

TYTELL, E.D. & LAUDER, G.V. 2004 The hydrodynamics of eel swimming: I. Wake structure. *J. Expl Biol.* **207**, 1825–1841.

VIRK, D., HUSSAIN, F. & KERR, R.M. 1995 Compressible vortex reconnection. *J. Fluid Mech.* **304**, 47–86.

VISBAL, M., YILMAZ, T.O. & ROCKWELL, D. 2013 Three-dimensional vortex formation on a heaving low-aspect-ratio wing: computations and experiments. *J. Fluids Struct.* **38**, 58–76.

VISBAL, M.R. 2009 High-fidelity simulation of transitional flows past a plunging airfoil. *AIAA J.* **47** (11), 2685–2697.

WILLIAMSON, C.H.K. & ROSHKO, A. 1988 Vortex formation in the wake of an oscillating cylinder. *J. Fluids Struct.* **2**, 355–381.

ZHU, Q. & SHOELE, K. 2008 Propulsion performance of a skeleton-strengthened fin. *J. Expl Biol.* **211**, 2087–2100.